



Computational Aerodynamic Simulations of a 1484 ft/sec Tip Speed Quiet High-Speed Fan System Model for Acoustic Methods Assessment and Development

Daniel L. Tweedt
AP Solutions, Inc., Cleveland, Ohio

NASA STI Program . . . in Profile

Since its founding, NASA has been dedicated to the advancement of aeronautics and space science. The NASA Scientific and Technical Information (STI) program plays a key part in helping NASA maintain this important role.

The NASA STI Program operates under the auspices of the Agency Chief Information Officer. It collects, organizes, provides for archiving, and disseminates NASA's STI. The NASA STI program provides access to the NASA Aeronautics and Space Database and its public interface, the NASA Technical Reports Server, thus providing one of the largest collections of aeronautical and space science STI in the world. Results are published in both non-NASA channels and by NASA in the NASA STI Report Series, which includes the following report types:

- **TECHNICAL PUBLICATION.** Reports of completed research or a major significant phase of research that present the results of NASA programs and include extensive data or theoretical analysis. Includes compilations of significant scientific and technical data and information deemed to be of continuing reference value. NASA counterpart of peer-reviewed formal professional papers but has less stringent limitations on manuscript length and extent of graphic presentations.
- **TECHNICAL MEMORANDUM.** Scientific and technical findings that are preliminary or of specialized interest, e.g., quick release reports, working papers, and bibliographies that contain minimal annotation. Does not contain extensive analysis.
- **CONTRACTOR REPORT.** Scientific and technical findings by NASA-sponsored contractors and grantees.

- **CONFERENCE PUBLICATION.** Collected papers from scientific and technical conferences, symposia, seminars, or other meetings sponsored or cosponsored by NASA.
- **SPECIAL PUBLICATION.** Scientific, technical, or historical information from NASA programs, projects, and missions, often concerned with subjects having substantial public interest.
- **TECHNICAL TRANSLATION.** English-language translations of foreign scientific and technical material pertinent to NASA's mission.

Specialized services also include creating custom thesauri, building customized databases, organizing and publishing research results.

For more information about the NASA STI program, see the following:

- Access the NASA STI program home page at <http://www.sti.nasa.gov>
- E-mail your question to help@sti.nasa.gov
- Fax your question to the NASA STI Information Desk at 443-757-5803
- Phone the NASA STI Information Desk at 443-757-5802
- Write to:
STI Information Desk
NASA Center for AeroSpace Information
7115 Standard Drive
Hanover, MD 21076-1320



Computational Aerodynamic Simulations of a 1484 ft/sec Tip Speed Quiet High-Speed Fan System Model for Acoustic Methods Assessment and Development

Daniel L. Tweedt
AP Solutions, Inc., Cleveland, Ohio

Prepared under Contract NNC06BA07B, Task NNC07E190T

National Aeronautics and
Space Administration

Glenn Research Center
Cleveland, Ohio 44135

Trade names and trademarks are used in this report for identification only. Their usage does not constitute an official endorsement, either expressed or implied, by the National Aeronautics and Space Administration.

Level of Review: This material has been technically reviewed by NASA technical management OR expert reviewer(s).

Available from

NASA Center for Aerospace Information
7115 Standard Drive
Hanover, MD 21076-1320

National Technical Information Service
5301 Shawnee Road
Alexandria, VA 22312

Available electronically at <http://www.sti.nasa.gov>

Computational Aerodynamic Simulations of a 1484 ft/sec Tip Speed Quiet High-Speed Fan System Model for Acoustic Methods Assessment and Development

Daniel L. Tweedt
AP Solutions, Inc.
Cleveland, Ohio 44135

Abstract

Computational Aerodynamic simulations of a 1484 ft/sec tip speed quiet high-speed fan system were performed at five different operating points on the fan operating line, in order to provide detailed internal flow field information for use with fan acoustic prediction methods presently being developed, assessed and validated. The fan system is a sub-scale, low-noise research fan/nacelle model that has undergone experimental testing in the 9- by 15-foot Low Speed Wind Tunnel at the NASA Glenn Research Center.

Details of the fan geometry, the computational fluid dynamics methods, the computational grids, and various computational parameters relevant to the numerical simulations are discussed. Flow field results for three of the five operating points simulated are presented in order to provide a representative look at the computed solutions.

Each of the five fan aerodynamic simulations involved the entire fan system, which includes a core duct and a bypass duct that merge upstream of the fan system nozzle. As a result, only fan rotational speed and the system bypass ratio, set by means of a translating nozzle plug, were adjusted in order to set the fan operating point, leading to operating points that lie on a fan operating line and making mass flow rate a fully dependent parameter. The resulting mass flow rates are in good agreement with measurement values.

Computed blade row flow fields at all fan operating points are, in general, aerodynamically healthy. Rotor blade and fan exit guide vane flow characteristics are good, including incidence and deviation angles, chordwise static pressure distributions, blade surface boundary layers, secondary flow structures, and blade wakes. Examination of the computed flow fields reveals no excessive or critical boundary layer separations or related secondary-flow problems, with the exception of the hub boundary layer at the core duct entrance. At that location a significant flow separation is present. The region of local flow recirculation extends through a mixing plane, however, which for the particular mixing-plane model used is now known to exaggerate the recirculation. In any case, the flow separation has relatively little impact on the computed rotor and FEGV flow fields.

Introduction

The development and validation of aircraft engine fan acoustic prediction methods is an important part of ongoing efforts by NASA and industry to reduce noise generation in the fan section of aircraft engines. This work is part of a larger task involving computational fluid dynamics (CFD) to simulate the aerodynamics of selected fan systems, each at several different operating points, for the purpose of providing detailed internal flow field information for use with fan acoustic prediction methods presently being developed, assessed and validated.

This report documents CFD work done on one of the selected fan systems, version II of the Quiet High-Speed (QHS) fan designed by Honeywell Corporation [1][†] with partial funding from NASA under the Advanced Subsonic Technology program. The QHS fan is a 22-inch sub-scale, low-noise research fan/nacelle model that has undergone experimental testing in the 9- by 15-foot Low Speed Wind Tunnel (LSWT) at the NASA Glenn Research Center.

[†] Numbers in square brackets indicate references.

Fan Geometry

A meridional plane drawing of the QHS fan system is shown in Figures 1a and 1b, with all major components depicted and shown to scale. The number of blades for each blade row is indicated in parenthesis, and the fan rotor blade stacking line is the zero-reference axial location. Downstream of the fan exit guide vane (FEGV) row the flow path splits to form a core duct and a bypass duct, which merge further downstream ahead of the exit nozzle. Support struts are located in the core and bypass ducts, near the flow path split. The rotating portion of the rotor hub includes the entire upstream centerbody/spinner, and extends about 0.150 inches downstream of the rotor to axial location 1.825 inches (see Figure 1b, mark below hub contour near rotor trailing edge).

The fan system bypass ratio (BPR) is controlled by the axial position of the nozzle centerbody, or so-called plug, which translates axially to adjust the flow area near the exit of the core duct, but without changing the flow area at the nozzle exit. Table 1 lists experimental and computational bypass ratios for corresponding nozzle plug positions. Note that a plug position of zero corresponds to a fully closed/blocked core duct, and that the computational BPR values were obtained by iteratively adjusting the plug position in order to achieve conditions close to the corresponding experimental BPR values.

Experimental testing of the QHS fan involved, in general, some different nozzle exit areas, each for essentially the same nozzle, but with the nozzle/nacelle trailing edge “trimmed” by different amounts. More trim provides a larger nozzle exit area, and different exit areas produce different fan operating lines. All experimental work relevant to the current task was done using a single trim configuration, denoted here as trim-1. To better match the experimental mass flow rates, however, a single non-experimental trim configuration, denoted as trim-A, was used for the computational simulations. In Figure 2 the geometry of the trim-A configuration is shown and compared to the trim-1 configuration. An untrimmed configuration, trim-0, is also shown for reference. Note that the nozzle exit area for trim-A is 0.26 percent less than that for trim-1.

Table 1: Nozzle Plug Positions and Corresponding Fan System Bypass Ratios

Operating Point	Rotational Speed (rpm)	Experimental Plug-Position (inches)	Computational Plug-Position (inches)	Experimental BPR	Computational BPR
SLTO	14,060	5.421	4.771	4.454	4.436
	13,280	4.931	4.541	4.581	4.615
Cutback	12,500	4.559	4.415	4.737	4.791
	10,935	4.180	4.171	4.977	4.965
Approach	9,840	3.959	4.083	5.100	5.085

Five aerodynamic simulation cases were defined for the QHS fan (see Table 1), each at a different rotational speed on the fan operating line. In all cases mechanical speed is equal to corrected speed since the far-field flow is at standard day sea-level total (stagnation) conditions. Rotor blade coordinates were provided for the running (hot) blade shape at the design rotational

speed, and no blade shape corrections were made for other rotational speeds. Note that the aerodynamic design point, with a rotational speed of 15621 rpm and a corresponding rotor blade tip speed of 1484 ft/sec, was not simulated.

Running rotor tip clearances were measured at blade leading edge, mid-chord, and trailing edge locations, over the entire range of rotational speeds, and quadratic regression curve fits of the measured data were used to determine the clearances at each of the selected rotational speeds. Table 2 summarizes these results. Quadratic functions defined from the data in Table 2 were used for calculating chordwise distributions of the tip clearance, which are shown in Figure 3.

Table 2: Rotor Blade Tip Clearances

Operating Point	Rotational Speed (rpm)	Leading Edge Tip Clearance (mils)	Mid-Chord Tip Clearance (mils)	Trailing Edge Tip Clearance (mils)
SLTO	14,060	33.92	26.00	26.70
	13,280	35.91	28.77	30.30
Cutback	12,500	37.74	31.43	33.86
	10,935	40.96	36.40	40.84
Approach	9,840	42.85	39.60	45.60

Computational Fluid Dynamics

Two different CFD codes were used to simulate the airflow around and through the fan system: an axisymmetric viscous solver called AVCS, and a three-dimensional viscous turbomachinery solver called TSWIFT. Multiple solution domains (grid blocks) were used, with axisymmetric solutions coupled to three-dimensional solutions at mixing planes by means of a separate computer program called SMPI, developed as a companion program for AVCS and TSWIFT. SMPI was also used to couple rotating and stationary three-dimensional solutions together at mixing planes. In general, the three-dimensional TWSIFT solver was used for computational domains in and near blade rows, and the axisymmetric AVCS solver was used for computational domains sufficiently far away from blade rows[†].

The AVCS and TSWIFT codes use similar numerical algorithms; both solve the Reynolds-averaged Navier-Stokes equations on body-fitted grids using an explicit, finite-difference scheme. The codes include viscous terms in the body-normal direction(s), but neglect them in the streamwise direction by applying the thin-layer approximation. The discretized equations are solved with a multi-stage Runge-Kutta time-marching scheme using a spatially varying time step, implicit residual smoothing, and preconditioning [2-5]. All simulations described herein were run

[†] All program-to-program communications, for mixing planes and direct block-to-block interfaces, were handled using a facility called SYNCEX (pronounced “sink-ex”). SYNCEX is a message-passing interface that enables two or more executing programs to efficiently exchange data on a single computer and/or over a network.

using a 2-stage Runge-Kutta scheme with a CFL number of 2.5, and using the AUSM+ upwind scheme [6] for best accuracy.

The TSWIFT code was derived from, and has the same basic features as the SWIFT code [7] developed by Chima at the NASA Glenn Research Center. TSWIFT also has a fairly general multiblock capability (when used with SYNCX; see preceding footnote), includes the two-equation SST turbulence model developed by Menter [8], and implements Giles' two-dimensional, steady-state, non-reflecting boundary conditions [9,10] at flow inlet, exit, and mixing-plane boundaries[†]. Note that when a two-equation turbulence model is used, either the Wilcox k - ω model [11] or the Menter SST model, it is necessary to pitchwise average the computed turbulence properties on the upstream side of the mixing plane. In that case the turbulence kinetic energy, k , and the ratio of turbulence kinetic energy to turbulence dissipation rate, k/ω , are each mass-averaged, and the resulting average values of k and (indirectly) ω are used as inflow boundary values for the domain on the downstream side of the mixing plane.

Computational Grids

An axisymmetric grid consisting of six two-dimensional grid blocks, shown in Figure 4, was used outside of the fan system blade rows. For clarity, only some of the grid lines are drawn in the figure, and the different blocks are shown in various colors: a far-field block (green), an external nacelle block (blue), an upstream/inlet block (black), a nozzle/downstream block (black), a bypass duct block (red), and a core duct block (magenta). The far-field block size is 193×45 nodes, the external nacelle block size is 361×65 nodes, the upstream/inlet block size is 185×85 nodes, the nozzle/downstream block size is 153×85 nodes, the bypass duct block size is 125×65 nodes, and the core duct block size is 137×49 nodes. The far-field block overlaps the top of the nacelle block, but the grid nodes are not aligned, so the computational solutions are interpolated there. The bottom of the nacelle block does not overlap the upstream/inlet and nozzle/downstream blocks, but the boundary-normal grid spacings are relatively small and the boundary nodes are aligned. The bypass and core duct blocks overlap the nozzle block, without nodal alignment, while along their common boundary they have nodal alignment but do not overlap each other.

The nacelle, inlet, duct, and nozzle grid blocks were all generated using a Poisson partial differential equation (PDE) solver, otherwise known as an elliptic grid generator, which produces grids with good boundary-normal node clustering and spacings, and generally good local orthogonality. Since the CFD method always directly includes the viscous sublayer in the near-wall treatment of turbulent boundary layers – wall functions are not used – the node spacings at solid walls are small. In the inlet and on the external surface of the nacelle the wall-normal spacing is nominally 0.0001 inches, whereas in the ducts and the nozzle the wall-normal spacing is nominally 0.0003 inches. Corresponding inner-variable wall distances, y^+ , are generally between 1.0 and 3.0.

Enlarged views of the two-dimensional grid in and around the fan system are shown in Figures 5a, 5b, and 5c, where every other grid line is drawn. In these figures the elliptic grid stretching for the nacelle, inlet, duct, and nozzle grid blocks can be seen more easily. Magnified views of the grid around the nacelle leading edge and trailing edge, with every grid line drawn, are shown in Figure 6.

[†] The SMPI code also implements Giles' two-dimensional, steady-state, non-reflecting boundary conditions.

Meridional locations of the three-dimensional blade row grid blocks are shown in Figure 7, with flow boundaries indicated by dashed and dash-dotted lines. The blue dash-dotted lines indicate grid block direct-interfaces, and the black dashed lines indicate mixing-plane interfaces. There are three primary grid blocks for the rotor: the rotor inlet H-grid block, the rotor blade row C-grid block, and the rotor exit H-grid block. The FEGV computational domain also involves three grid blocks: the FEGV C-grid block, the FEGV exit core H-grid block, and the FEGV exit bypass H-grid block. The red streamlines in Figure 7 show stream-surface locations for blade-to-blade (streamwise-pitchwise) grid views, as well as for blade-to-blade flow contour plots, to be shown later.

The blade row grids, except for the rotor exit and FEGV exit H-grid blocks, were generated using a computer program called TTGRID, which is a modified version of TCGRID [12], a grid generator for turbomachinery developed by Chima at the NASA Glenn Research Center. TTGRID applies an elliptic PDE solver to the blade-to-blade mesh surfaces of blade row C- and H-grids.

Meridional plane projections of the three-dimensional blade row grid blocks at grid surfaces located about mid-pitch between the blades are shown in Figure 8. Rotor grid blocks are drawn in black and green, the FEGV grid blocks are drawn in red and blue, and the core and bypass strut grid blocks are drawn in magenta. For clarity, only every other grid line in the streamwise direction (every fourth line for the rotor exit block) is shown, although all grid lines in the spanwise direction are drawn. Corresponding three-dimensional views of the grid blocks are provided in Figures 9 and 10 for the rotor and stator, respectively, again with only some of the grid lines drawn. The rotor C-grid (black) has a size of $185 \times 49 \times 85$ nodes, the rotor inlet H-grid (green) has a size of $25 \times 28 \times 85$ nodes, and the rotor exit H-grid (green) has a size of $97 \times 89 \times 81$ nodes. Note that the rotor inlet H-grid overlaps the rotor blade C-grid and has node-to-node alignment with it. The rotor exit H-grid also overlaps the rotor blade C-grid, but the grid nodes are not aligned. For the FEGV, the C-grid (red) has a size of $193 \times 45 \times 85$ nodes, the exit core H-grid (blue) has a size of $47 \times 89 \times 57$ nodes, and the exit bypass H-grid (blue) has a size of $47 \times 89 \times 73$ nodes. As with the rotor, the FEGV exit H-grids overlap the C-grid, but the grid nodes are not aligned. On their common boundary just upstream of the flow path splitter, the two FEGV exit H-grid blocks do not overlap each other, but the boundary-normal spacings are small and the nodes are aligned. Lastly, the core strut H-grid has a size of $97 \times 73 \times 49$ nodes, and the bypass strut H-grid has a size of $97 \times 81 \times 65$ nodes. All of the three-dimensional grids have boundary-normal node spacings which are nominally 0.0002 inches at blade/vane surfaces, and 0.0003 inches at endwall surfaces.

Streamwise-pitchwise views of the rotor grid at three spanwise locations, corresponding to the red streamlines in Figure 7, are shown in Figure 11 with every other grid line drawn (every fourth line in the streamwise direction for the exit H-grid block). Corresponding pitchwise-spanwise views of the rotor C-grid and exit H-grid at the respective block downstream boundaries are shown in Figure 12.

Over the rotor blade tip, in the endwall clearance gap, an O-grid block of size $179 \times 13 \times 17$ nodes is used. The tip clearance grid is shown in Figure 13, where magnified views around the blade leading- and trailing-edges are included, as well as a magnified axial cross-section view near mid-chord. All grid lines are drawn for the magnified views. Note that the tip clearance grid overlaps the rotor blade C-grid and has node-to-node alignment with it.

A streamwise-pitchwise view of the FEGV grid near midspan, corresponding to the middle red streamline in Figure 7, is shown in Figure 14. Shown below the full view are magnified views of the vane leading and trailing edge regions. In the full view, for clarity, only every other grid line

parallel to the vane surface is drawn for the C-grid block (red), and every other line in both grid directions is drawn for the exit H-grid block (blue). Corresponding pitchwise-spanwise views of the FEGV C-grid and exit H-grid at the block downstream boundaries are shown in Figure 15.

A streamwise-pitchwise view of the core-strut grid near midspan, with magnified views of the strut leading and trailing edge regions, is shown in Figure 16. Midspan in this case corresponds to the lower red streamline in Figure 7. Because the bypass-strut H-grid is similar to the core-strut H-grid, only one of them is shown for the blade-to-blade view. Views of both grids at the block downstream boundaries, however, are shown in Figure 17.

All computational grid blocks and their respective sizes are summarized below in Tables 3 and 4.

Table 3: Two-Dimensional Grid Blocks

Grid Block	Size (I×J×K)	Number of Nodes
Fan System Upstream/Inlet	185×85	15,725
Fan System Nozzle/Downstream	153×85	13,005
Fan System Core Duct	137×49	6,713
Fan System Bypass Duct	125×65	8,125
Fan System External Nacelle	361×65	23,465
Fan System Far Field	193×45	8,685
Total All Blocks		75,718

Table 4: Three-Dimensional Grid Blocks

Grid Block	Size (I×J×K)	Number of Nodes
Rotor Inlet H-Grid	25×28×85	59,500
Rotor Blade C-Grid	185×49×85	770,525
Rotor Exit H-Grid	97×89×81	699,273
Rotor Tip Clearance O-Grid	149×13×17	32,929
FEGV C-Grid	193×45×85	738,225
FEGV Exit Core H-grid	47×89×57	238,431
FEGV Exit Bypass H-grid	47×89×73	305,359
Core Strut H-grid	97×73×49	346,969
Bypass Strut H-grid	97×81×65	510,705
Total All Blocks		3,701,916

To conclude this section, the rotor exit H-grid block and its relative importance to the CFD solutions will be discussed. It is perhaps apparent that this grid block involves a relatively large number of grid nodes, even though it contains no blade surfaces and is essentially just a downstream extension of the rotor blade C-grid. The higher grid density is necessary, however, to provide the numerical resolution needed for accurate wake convection, and to achieve a reasonable level of grid independence for the CFD solution. If the grid is too coarse, particularly in regions where the flow field involves large gradients and the primary flow is not aligned with the grid, then numerical dissipation is excessive and causes substantial distortion of computed local flow features. More specifically, excess artificial dissipation causes the computed wake and blade tip vortex to decay too rapidly.

If the primary purpose of the CFD simulations were only aerodynamic performance assessment and/or prediction, then the lack of local flow field accuracy in the wake region might not be crucial because local accuracy typically has a relatively small influence on spatially averaged performance quantities. For the current task, however, the computed rotor wake and tip-vortex structures are important because they define flow field characteristics associated with noise generation. Particularly important are the computed flow field results at the rotor exit H-grid exit boundary (and mixing plane) since these are intended for direct use in acoustic methods assessment, research and development.

Fan System Aerodynamic Simulations

All CFD simulations were run with the far-field (free stream, flight) Mach number set at 0.100, with total (stagnation) conditions set at standard day sea-level values. The corresponding unit Reynolds number is $5.915\text{E}+05$ inches⁻¹. Air is modeled as a perfect gas with a ratio of specific heats, γ , equal to 1.400.

The effects of turbulence were modeled using the two-equation SST turbulence model [8], with free stream turbulence on the far-field upstream boundary set at 0.2 percent, along with a turbulence (eddy) viscosity equal to 0.2 times the molecular viscosity, giving a turbulence length scale of $1.39\text{E}-03$ inches. The corresponding turbulence kinetic energy is $5.99\text{E}-08$ (dimensionless; multiply by square of free stream stagnation speed-of-sound to obtain a dimensional value)[†]. In all the cases simulated, rotor blade laminar-to-turbulent boundary layer transition occurred near the leading edge, at a location around 5 percent of blade chord.

Measured and computed values of the fan mass flow rate are listed below in Table 5. All five of the CFD simulation cases were run until the maximum and average (RMS) solution residuals were reduced by 4 to 5 orders of magnitude. Similar levels of convergence were obtained for performance-related quantities such as mass flow rate, average total temperature, and average total pressure. Integrated mass flow conservation discrepancies for the computed solutions are fairly small, being normally less than ± 0.07 percent at all mixing planes. At the two lowest rotational speeds, however, the discrepancies for mixing planes downstream of the splitter are a

[†] At the fan inlet the turbulence is lower than originally intended because of turbulence decay upstream of the inlet, and because of an error in calculating the inlet boundary values so as to account for that decay. The turbulence is not so low, however, that it significantly affects the computed aerodynamics. Turbulence at the fan inlet is nominally about 0.03 percent, with a turbulence viscosity of 0.2 times the molecular viscosity and a turbulence kinetic energy of around $3.5\text{E}-08$.

little larger: around -0.08 percent for the 10935 rpm operating point, and -0.13 percent for 9840 rpm operating point.

Table 5: Measured and Computed Fan Flow Rates

Operating Point	Rotational Speed (rpm)	Measured Flow Rate (lbm/sec)	Computed Flow Rate (lbm/sec)	Flow Rate Difference (percent)
SLTO	14,060	89.64	89.71	0.08
	13,280	84.03	84.12	0.11
Cutback	12,500	78.79	78.58	-0.27
	10,935	68.21	68.07	-0.21
Approach	9,840	61.00	60.80	-0.33

The measured and computed mass flow rates in Table 5 differ by -0.33 to 0.11 percent, depending on operating point. The uncertainty in measured flow rate is estimated to be around ± 0.5 percent. Recall that the nozzle exit area was adjusted by changing the amount of nacelle trailing-edge trim, to better match the computed and experimental flow rates. The adjustment, determined only at the SLTO operating point, is relatively small, however, with the computational model having only 0.26 percent less nozzle exit area than the experimental model.

Selected results from three of the five CFD simulation cases are presented below. Flow field contour plots are presented for results at the SLTO, cutback, and approach operating points, the primary purpose being to provide a representative look at the computed solutions. More extensive and detailed flow field information can be obtained directly from the CFD grid and solution data sets, which are being made available along with this report, or which can be obtained separately upon request.

Mach number contours for the entire fan system flow field at the SLTO operating point are shown in Figure 18, where the three-dimensional blade-row solutions have been mixed-out averaged in the pitchwise direction. An enlarged view of the fan region is shown in Figure 19, and a corresponding contour plot of turbulence kinetic energy, mass-averaged in the pitchwise direction, is shown in Figure 20.

Notice in Figure 19 that the hub boundary layer for the (pitchwise-averaged) flow at the core duct entrance is separated, with the region of reversed flow extending from just upstream of the core entrance mixing plane to about the leading edge of the core strut. The separation starts in the FEGV computational domain, is highly three-dimensional, and extends in the circumferential direction over only part of the vane pitch. The occurrence of recirculating flow at the mixing plane, with flow traversing the plane both ways at particular spanwise locations, presented a significant challenge for the mixing-plane computational model. Although the difficulty has since been resolved, at the time of the simulations it was handled using only a marginally acceptable scheme. Consequently, as is now known, the computed flow recirculation is artificially excessive, or exaggerated. Its impact, however, on the overall simulated solutions is relatively minor, in large part because the flow separation has little effect on the fan rotor and stator flow fields.. Even at the

lower fan rotational speeds and flow rates, where the computed recirculation zone is markedly larger, the computed fan solutions are considered to be only minimally compromised. Perhaps of greater significance is the observation that system bypass ratio was fairly sensitive to the severity of the flow separation, making it difficult to closely match (by adjusting the nozzle plug position) computational values to experimental ones. This may explain, at least in part, the different experimental and computational plug positions at each operating point (see Table 1).

Rotor blade-to-blade relative (rotating system) Mach number contours at the SLTO operating point are shown in Figures 21a and 21b. Figure 21a shows a near tip section at about 87 percent span from the hub, and Figure 21b shows near midspan and near hub sections at about 52 and 15 percent span, respectively (see red streamlines in Figure 7). Relative Mach number contours in and around the rotor tip endwall clearance gap are shown in Figure 22, where the tip mid-clearance-gap location is roughly 0.020 inches from the casing endwall, and the mid-chord axial location is 0.400 inches upstream of the rotor blade stacking line. Corresponding contours of relative Mach number at the rotor C-grid downstream boundary, located nominally 0.400 inches downstream of the rotor trailing edge (0.300 at hub to 0.500 at tip), are shown in Figure 23, and contours of various flow properties at the rotor exit bypass H-grid downstream boundary, which is the downstream mixing plane located nominally 0.350 inches upstream of the FEGV leading edge (0.250 at hub to 0.450 at tip), are shown in Figures 24a and 24b. Figure 24a shows relative and absolute (stationary system) Mach number contours, and Figure 24b shows entropy and turbulence kinetic energy contours. Note that entropy is non-dimensionalized by the gas constant, R , and is zero at the upstream reference condition.

FEGV blade-to-blade absolute Mach number contours for operation at the SLTO operating point are shown in Figures 25a and 25b. Figure 25a shows a vane section at about 87 percent span from the hub, and Figure 25b shows vane sections at about 52 and 15 percent span (see red streamlines in Figure 7). Corresponding Mach number contours at the FEGV C-grid downstream boundary and exit H-grid downstream boundary, respectively, are shown in Figures 26 and 27.

Bypass strut blade-to-blade absolute Mach number contours for a location near midspan (see middle red streamline in Figure 7), for operation at the SLTO operating point, are shown in Figure 28. Corresponding Mach number contours at the strut grid downstream boundary are shown in Figure 29. Mach contours for the core-strut downstream boundary are included in Figure 29.

Mach number contours for the entire fan system at the cutback operating point are shown in Figure 30, with an enlarged view of the fan region shown in Figure 31. Again, the three-dimensional blade-row solutions have been mixed-out averaged in the pitchwise direction. Corresponding rotor blade-to-blade relative Mach number contours are shown in Figures 32a and 32b, and various flow property contours at the rotor downstream mixing plane are shown in Figures 33a and 33b. Flow field contours for the FEGV at cutback operation are not shown, but are in general aerodynamically similar to those at SLTO.

Mach number contours for the entire fan system at the approach operating point are shown in Figure 34, and Figure 35 shows an enlarged view of the fan region. Corresponding rotor blade-to-blade relative Mach number contours are shown in Figures 36a and 36b, and various flow property contours at the rotor downstream mixing plane are shown in Figures 37a and 37b. Absolute Mach number contours for the FEGV are shown in Figures 38a and 38b, and in Figures 39 and 40. The computed FEGV flow field, like that for cutback operation, is aerodynamically similar to the SLTO solution, at least generally. Notice in Figure 38a, however, the flow separation from the vane pressure side for the near tip section. This separation, caused by

a locally negative vane incidence, is not aerodynamically critical, but does increase the vane total-pressure loss slightly. A similar, but less severe separation is also present in the FEGV solution for the cutback operating point, while for the SLTO operating point (see Figure 25a) the separation is relatively minor. Nevertheless, despite this non-conformity and other differences, the solutions can be considered aerodynamically similar overall, showing that the FEGV flow field scales more-or-less with flow rate for all simulated operating points on the fan operating line.

Finally, by comparing Figure 35 to Figure 19, it can be seen that the hub flow separation at the core duct entrance is larger for the approach operating point (also for the cutback operating point; compare Figure 31 to Figure 19) than for the SLTO operating point. This difference, which was alluded to earlier in the discussion of SLTO results, can also be seen in more detail, as well as from a more three-dimensional perspective, by comparing Figure 40 to Figure 27. These latter figures allow the non-averaged flow fields at the FEGV downstream mixing plane to be contrasted.

Concluding Remarks

The entire fan system was aerodynamically simulated for five operating points, requiring only fan rotational speed and nozzle plug position to be adjusted as the independent parameters when setting each operating point. As a result, the computed operating points lie on a fan operating line, and mass flow rate is a dependent parameter. The comparison of computed and measured fan system mass flow rates are in good agreement, indicating indirectly that the computational and experimental fan operating lines are nearly the same.

The computed blade row flow fields at all operating points are, in general and as expected, aerodynamically healthy. Rotor blade and FEGV flow characteristics are good, including incidence and deviation angles, chordwise static pressure distributions (not shown, but can be inferred from Mach number distributions), blade surface boundary layers, secondary flow structures, and blade wakes. Examination of the computed flow fields reveals no excessive or critical boundary layer flow separations or related secondary flow problems, with the exception of the hub boundary layer at the core duct entrance. At that location a significant flow separation is present. The region of local flow recirculation extends through a mixing plane, however, which for the particular mixing-plane model used is now known to exaggerate the recirculation. In any case, the flow separation has relatively little impact on the computed rotor and FEGV flow fields.

References

1. Kontos, Karen, Weir, Don, and Ross, David, "Quiet High Speed Fan II (QHSF II) Final Report," NASA CR-2012-217451, March 2012.
2. Chima, R. V., "Viscous Three-Dimensional Calculations of Transonic Fan Performance," in CFD Techniques for Propulsion Applications, AGARD Conference Proceedings No. CP-510, AGARD, Neuilly-Sur-Seine, France, February 1992, pp 21-1 to 21-19 (also NASA TM-103800).
3. Chima, R. V., and Yokota, J. W., "Numerical Analysis of Three-Dimensional Viscous Flows in Turbomachinery," AIAA Journal, Vol. 28, No. 5, May 1990, pp. 798-806.
4. Tweedt, Daniel L., and Chima, Rodrick V., "Rapid Numerical Simulation of Viscous Axisymmetric Flow Fields," NASA TM-107103 (also AIAA-96-0449), November 1995.
5. Tweedt, Daniel L., Chima, Rodrick V., and Turkel, Eli, "Preconditioning for Numerical Simulation of Low Mach Number Three-Dimensional Viscous Turbomachinery Flows," NASA TM-113120 (also ICOMP-97-11 and AIAA-97-1828), October 1997.
6. Chima, R. V. and Liou, M.-S., "Comparison of the AUSM+ and H-CUSP Schemes for Turbomachinery Applications," AIAA Paper AIAA-2003-4120 (also NASA TM-2003-212457).
7. Chima, R. V., "Swift – Multiblock Analysis Code for Turbomachinery," User's Manual and Documentation, Version 300, August 2003.
8. Menter, R. F., "Two-Equation Eddy-Viscosity Turbulence Models for Engineering Applications," AIAA Journal, Vol. 32, No. 8, August 1994, pp. 1598-1605 (also NASA TM-111958).
9. Giles, Michael B., "Nonreflecting Boundary Conditions for Euler Equation Calculations," AIAA Journal, Vol. 28, No. 12, December 1990, pp. 2050-2058.
10. Giles, Michael, "UNSFLO: A Numerical Method For The Calculation Of Unsteady Flow In Turbomachinery," GTL Report No. 205, May 1991, pp. 45-56.
11. Wilcox, David C., *Turbulence Modeling for CFD*, DCW Industries, Inc., La Cañada, CA, Third edition, 2006.
12. Chima, R. V., "TCGRID 3-D Grid Generator for Turbomachinery, User's Manual and Documentation," Version 300, July, 2003.

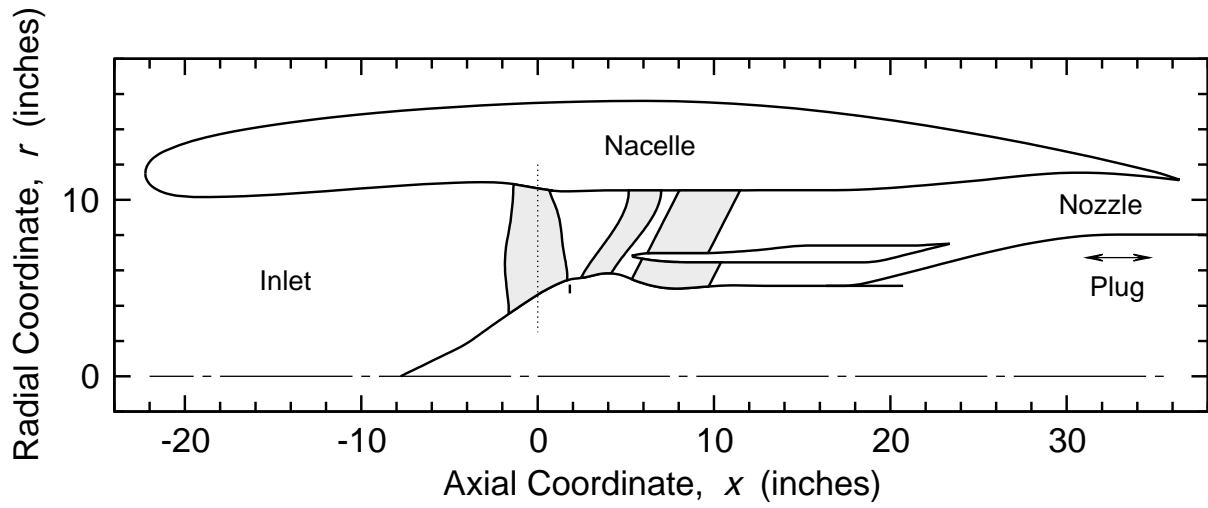


Figure 1a: Schematic Drawing of the QHS Fan System

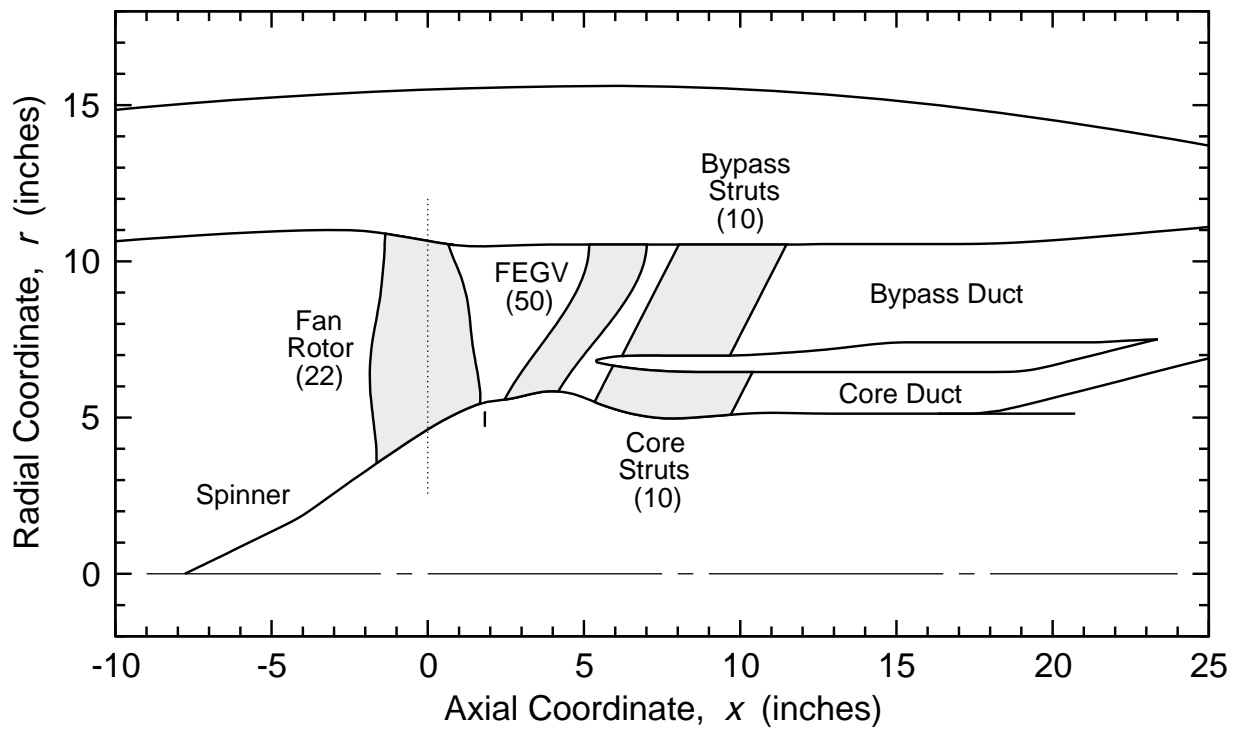


Figure 1b: Enlarged Partial Schematic Drawing of the QHS Fan System

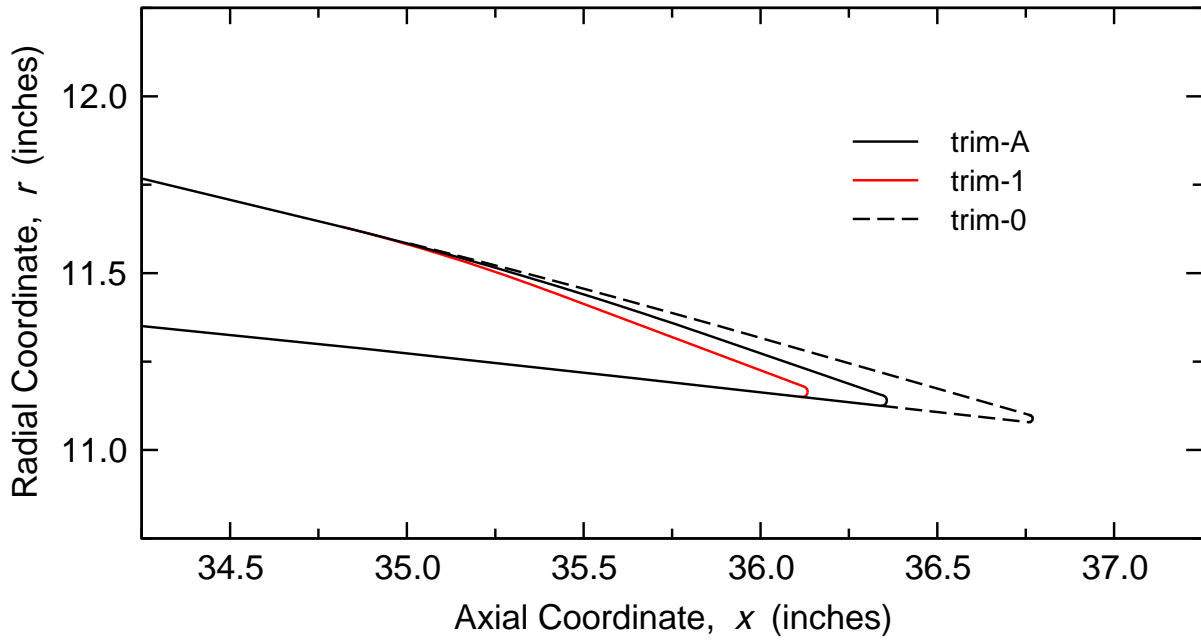


Figure 2: Nacelle Trailing Edge Trim Configurations

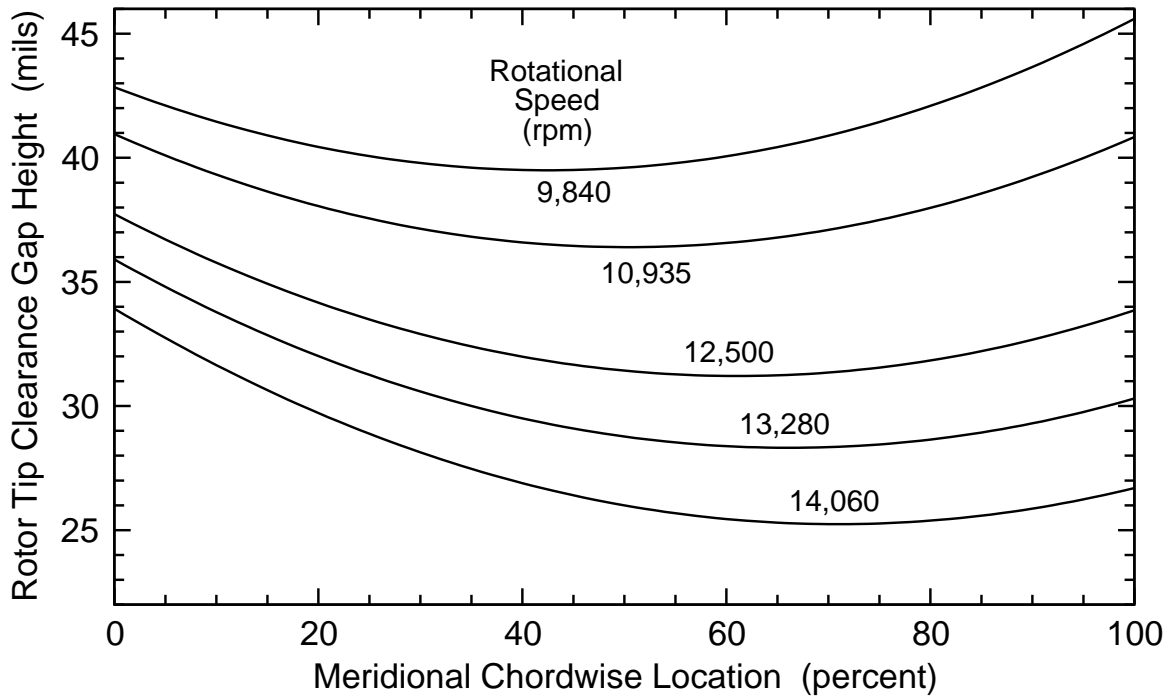


Figure 3: Chordwise Distributions of Rotor Blade Tip Clearance

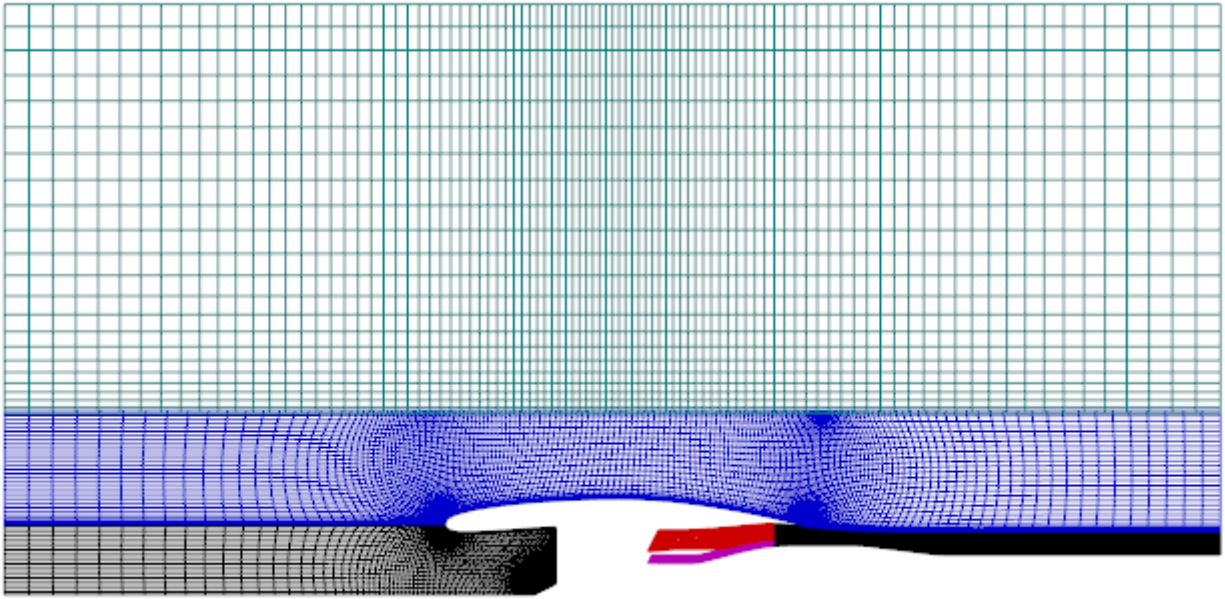


Figure 4: Two-Dimensional Axisymmetric CFD Grid Blocks (Entire Computational Domain)

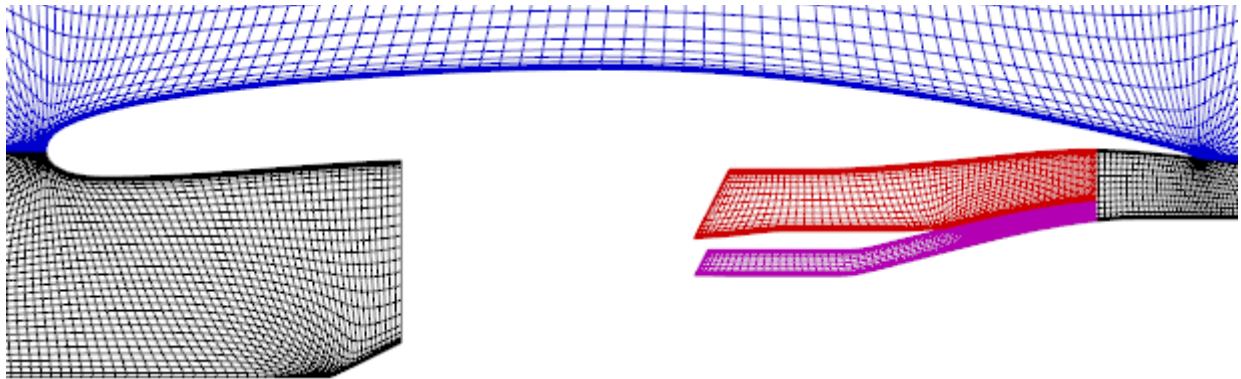


Figure 5a: Enlarged Inlet, Core and Bypass Duct, Nozzle, and Nacelle Grid Blocks

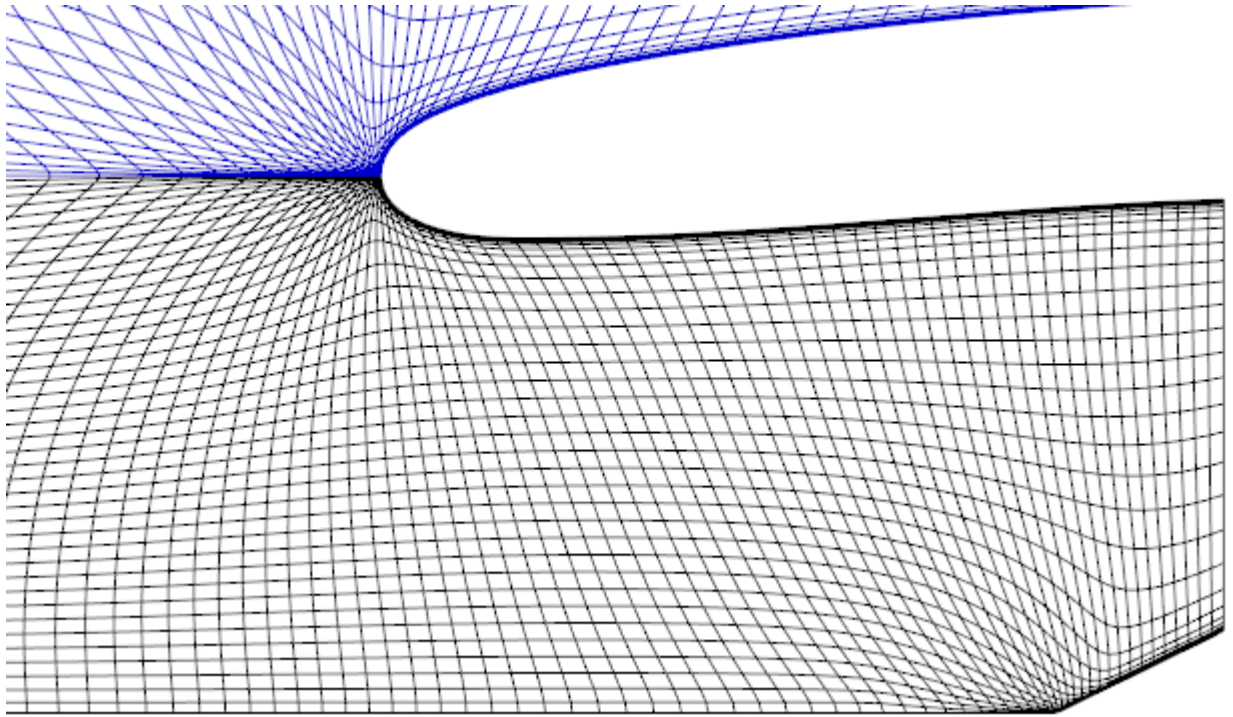


Figure 5b: Enlarged Inlet Grid Block

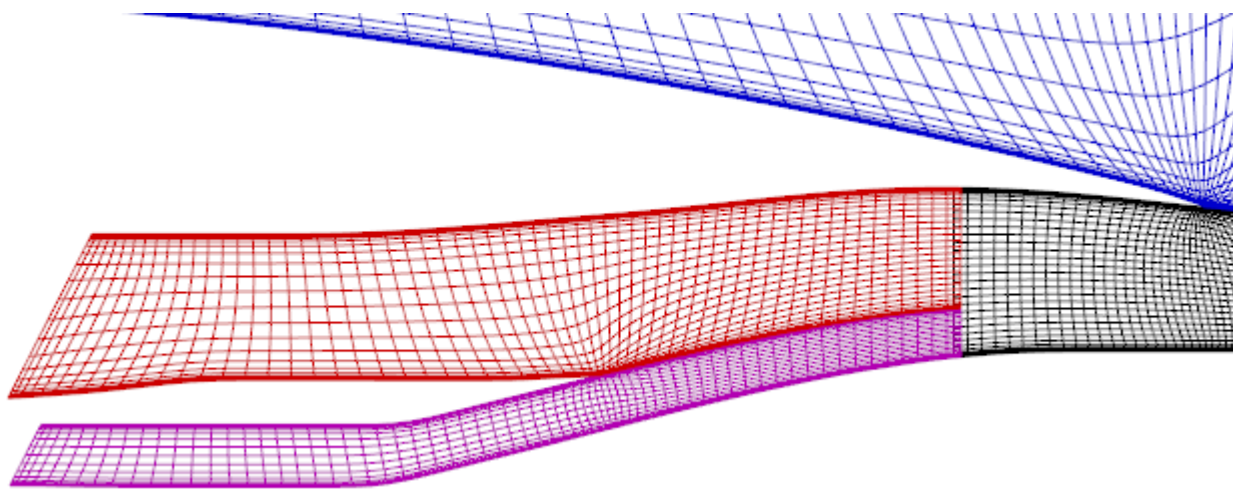


Figure 5c: Enlarged Duct and Nozzle Grid Blocks

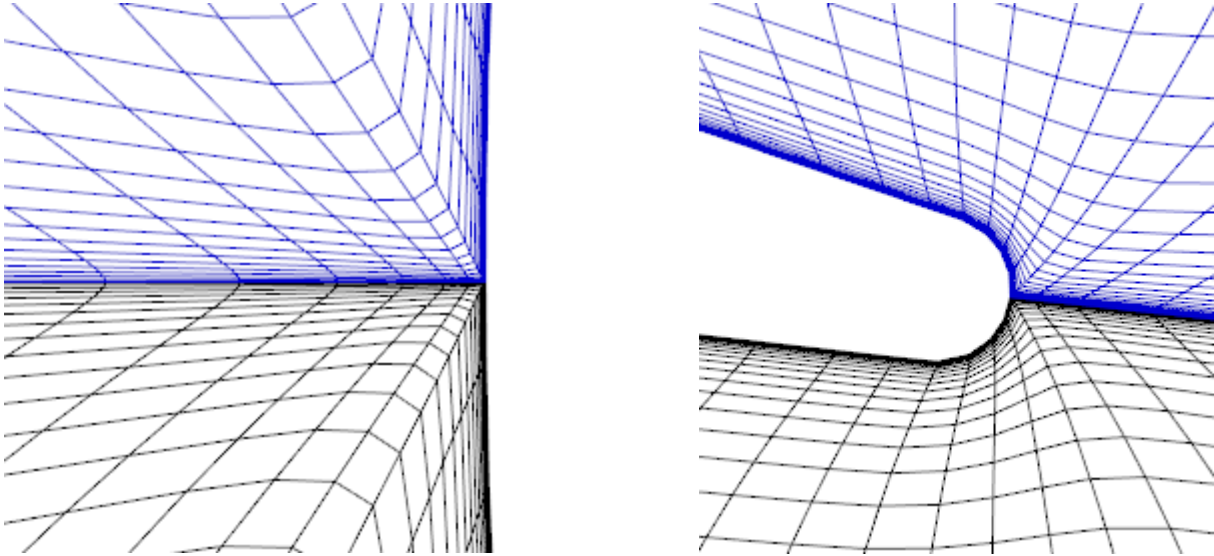


Figure 6: Magnified Nacelle Leading and Trailing Edge Grids

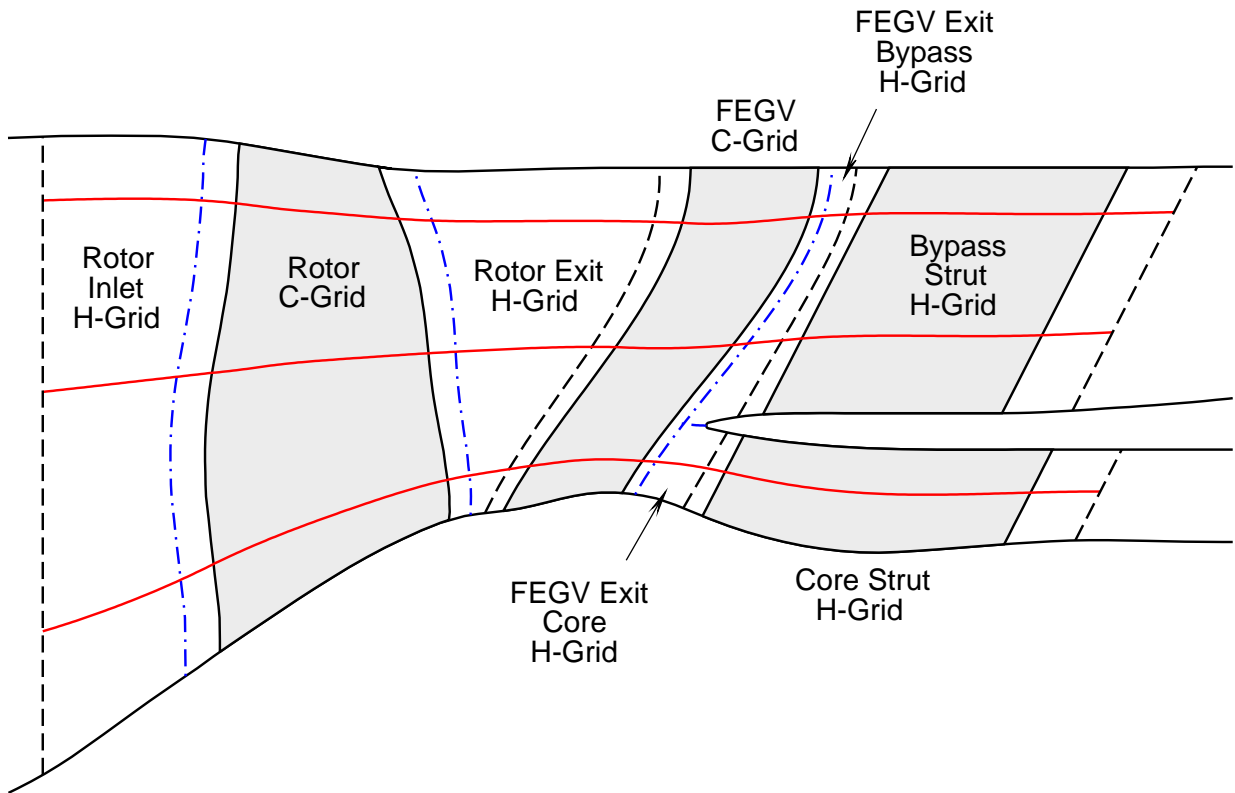


Figure 7: Meridional Location and Extent of Three-Dimensional CFD Grid Blocks

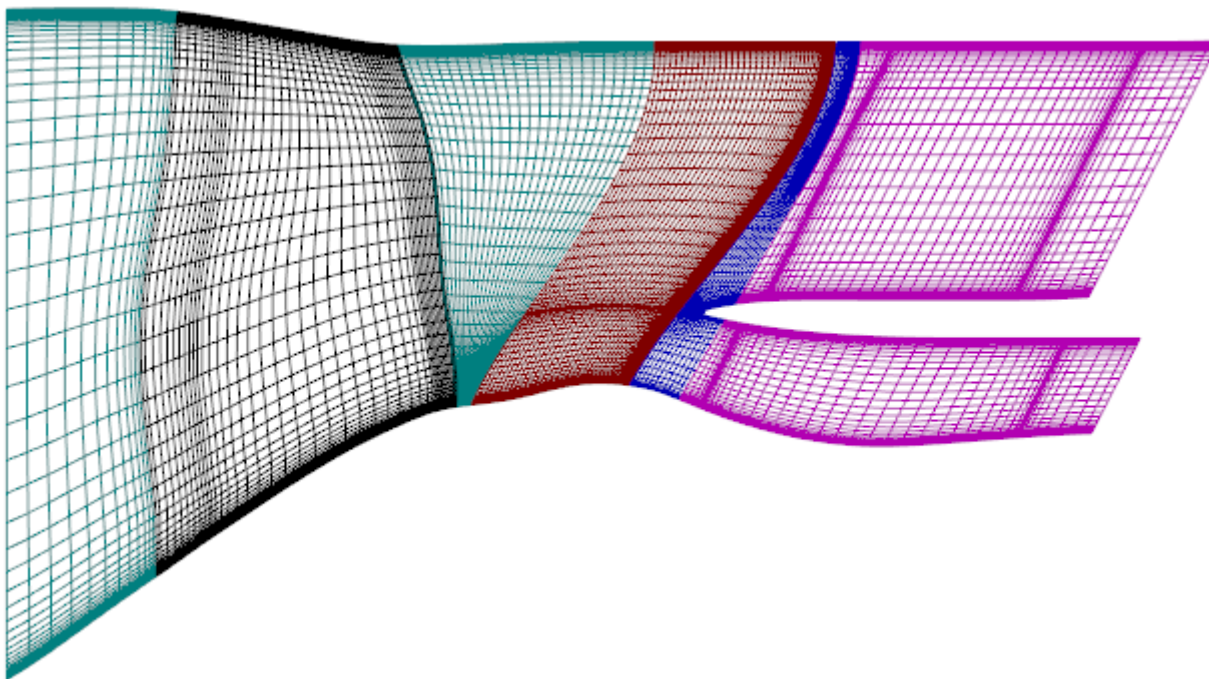


Figure 8: Meridional View of Three-Dimensional CFD Grid Blocks (Mid-Pitch Location)

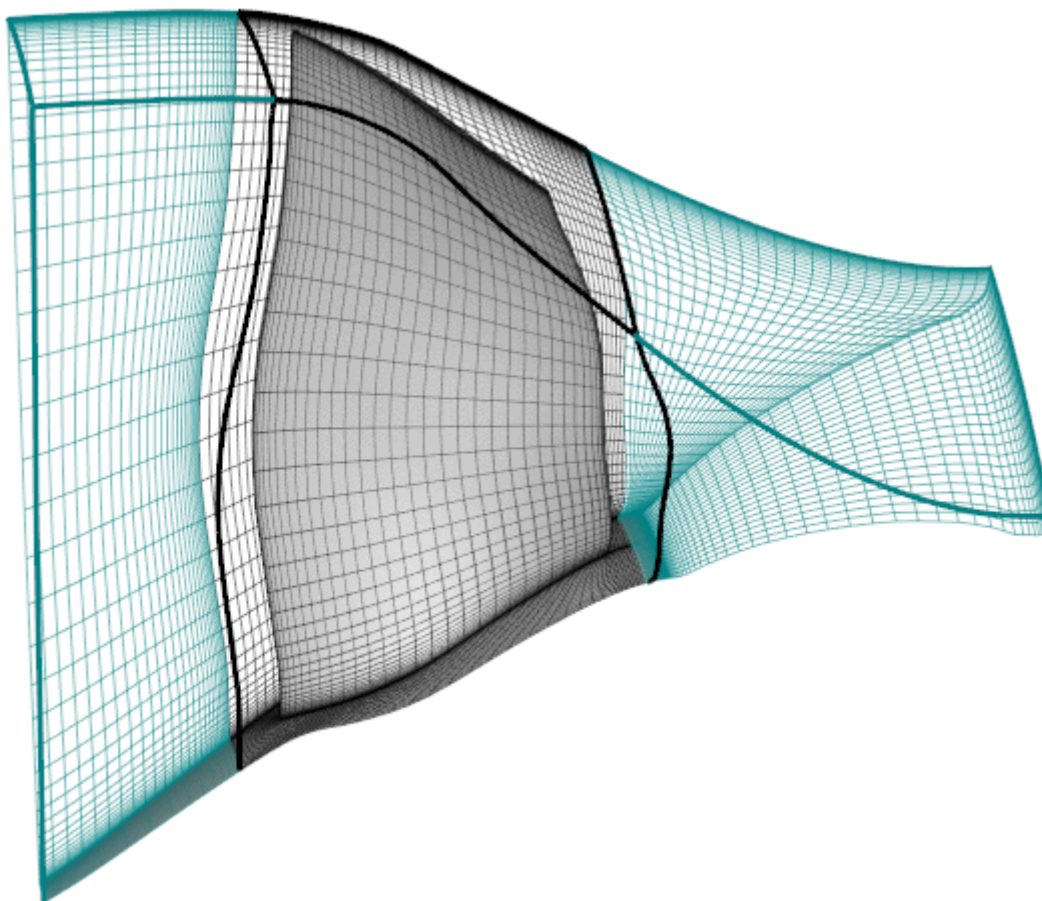


Figure 9: Three-Dimensional View of Rotor Grid

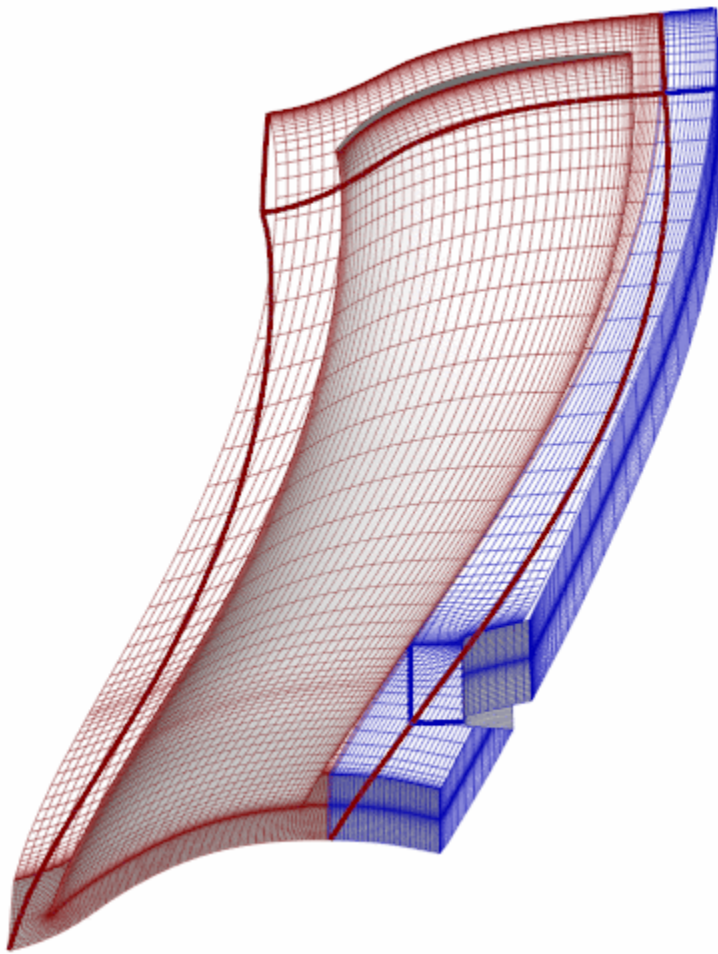


Figure 10: Three-Dimensional View of FEGV Grid

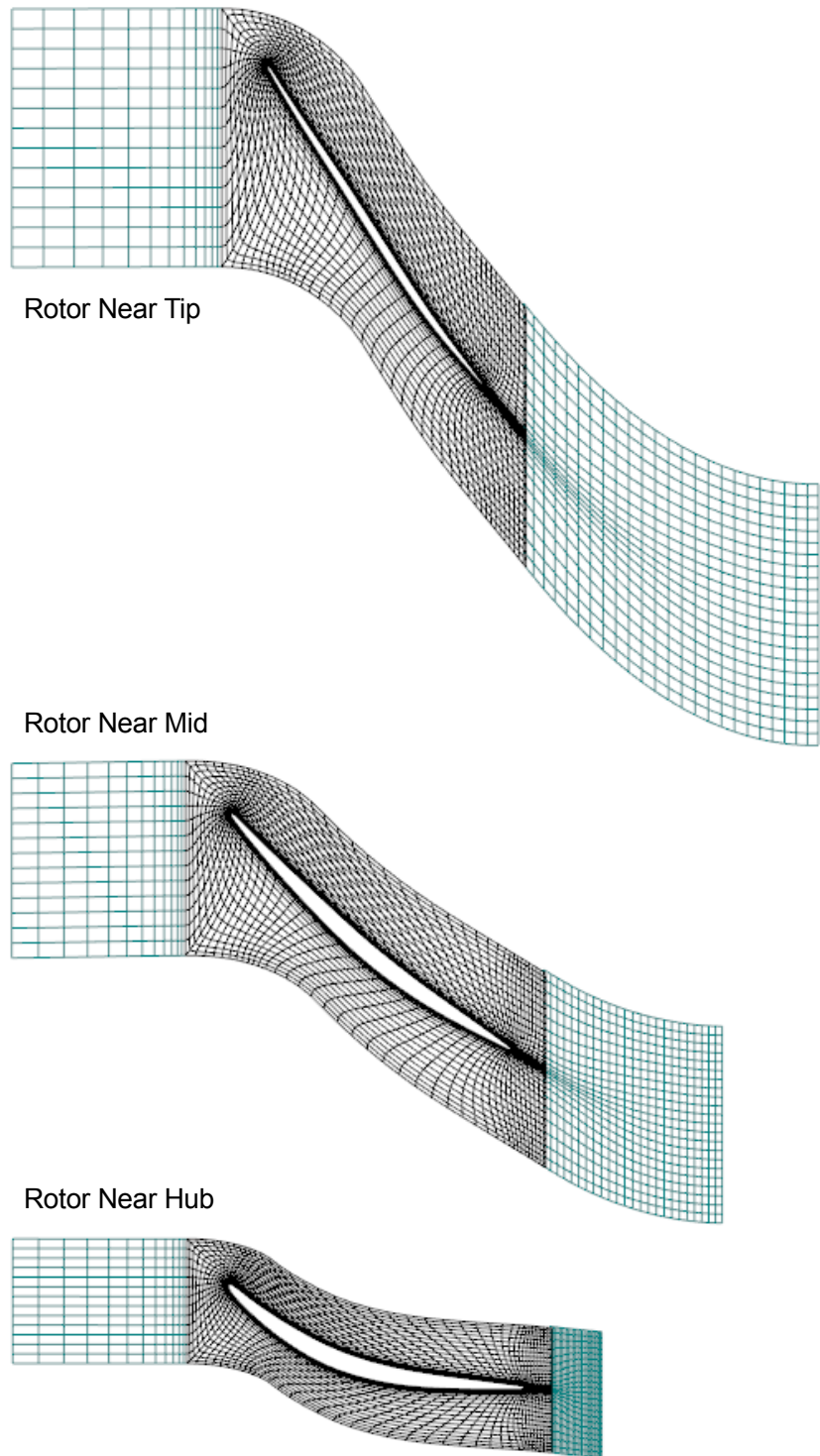


Figure 11: Rotor Grid at Three Spanwise Locations

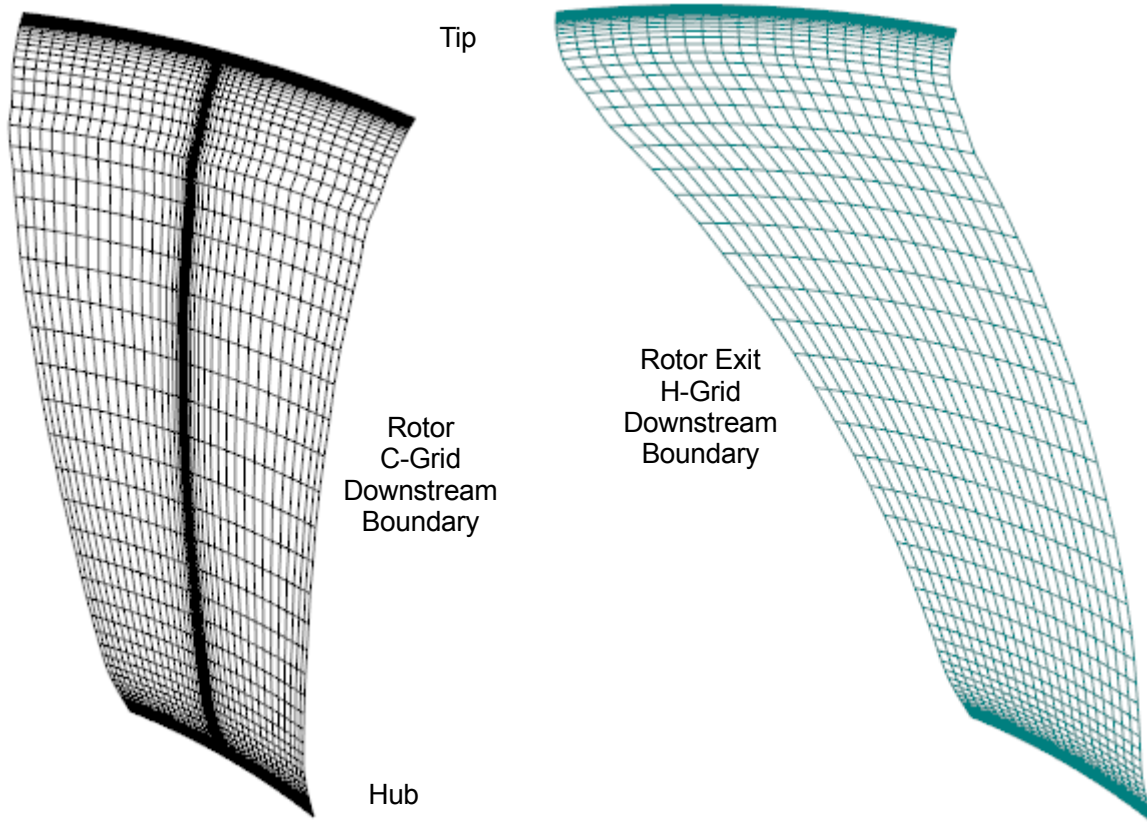


Figure 12: Rotor Grid at Block Downstream Boundaries

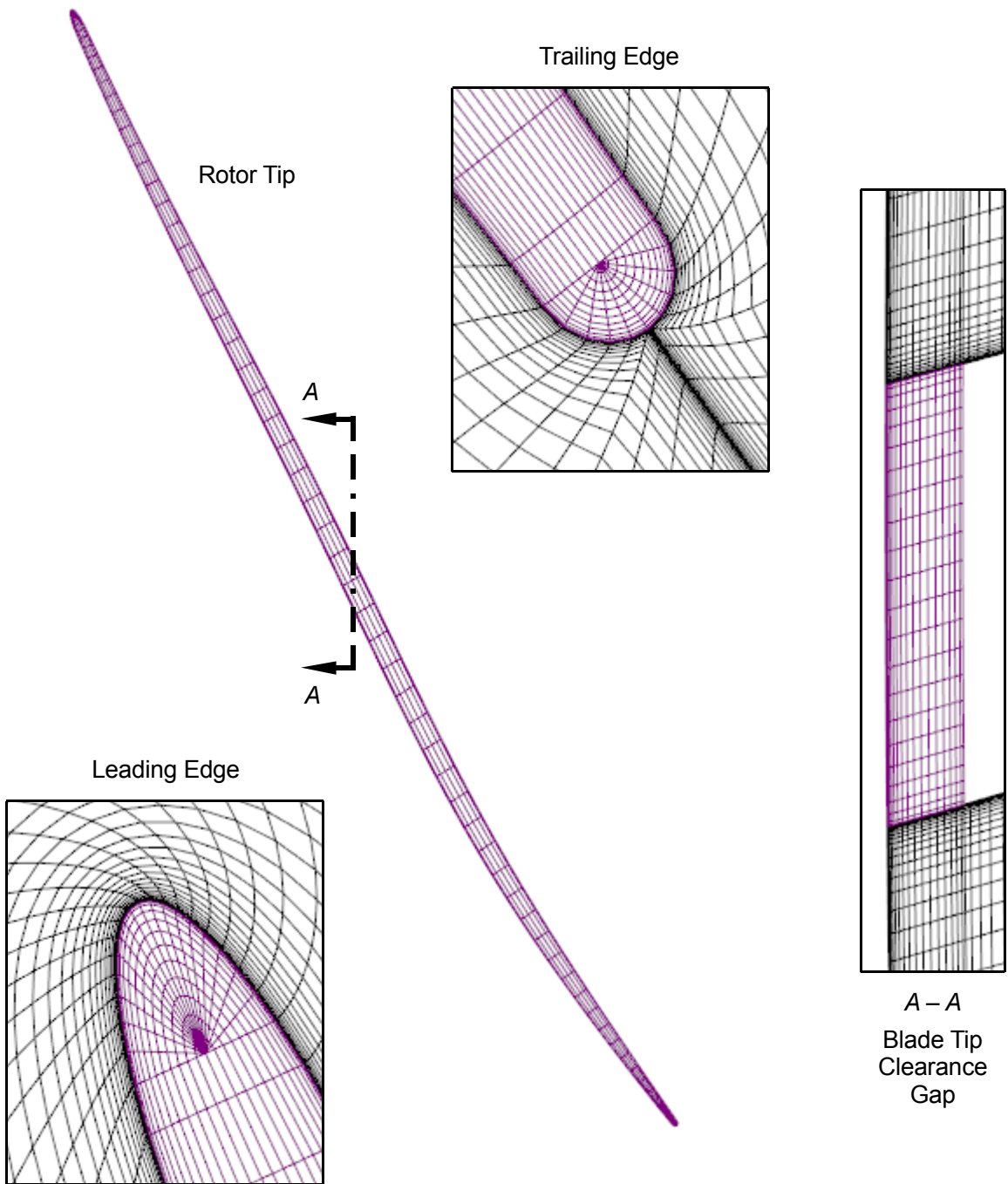
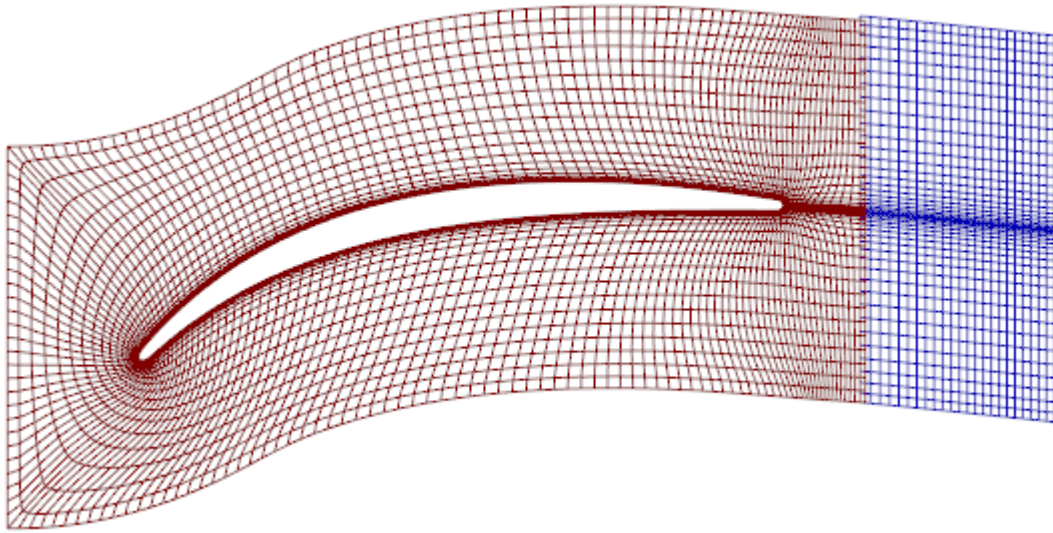
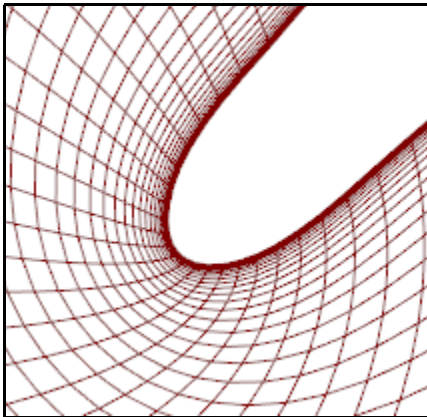


Figure 13: Rotor Tip Clearance Grid

FEGV Near Midspan



Leading Edge



Trailing Edge

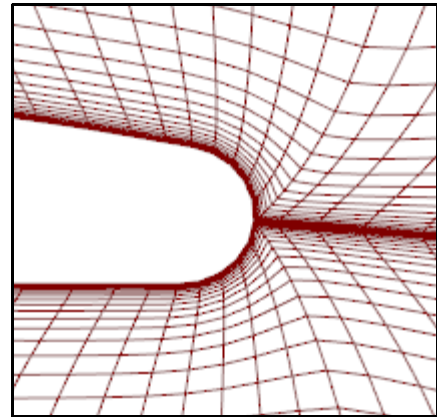


Figure 14: FEGV Grid at Near Midspan Location

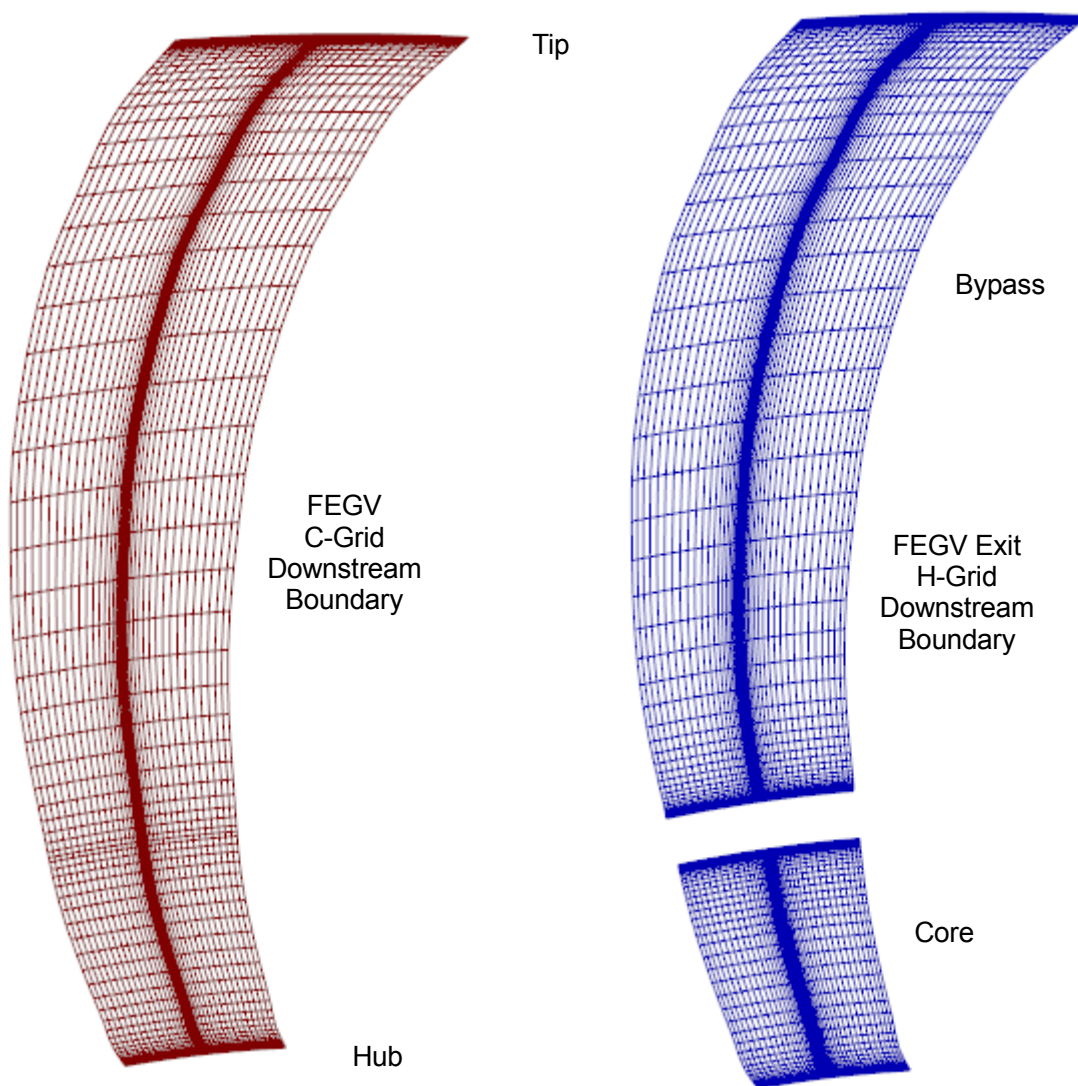
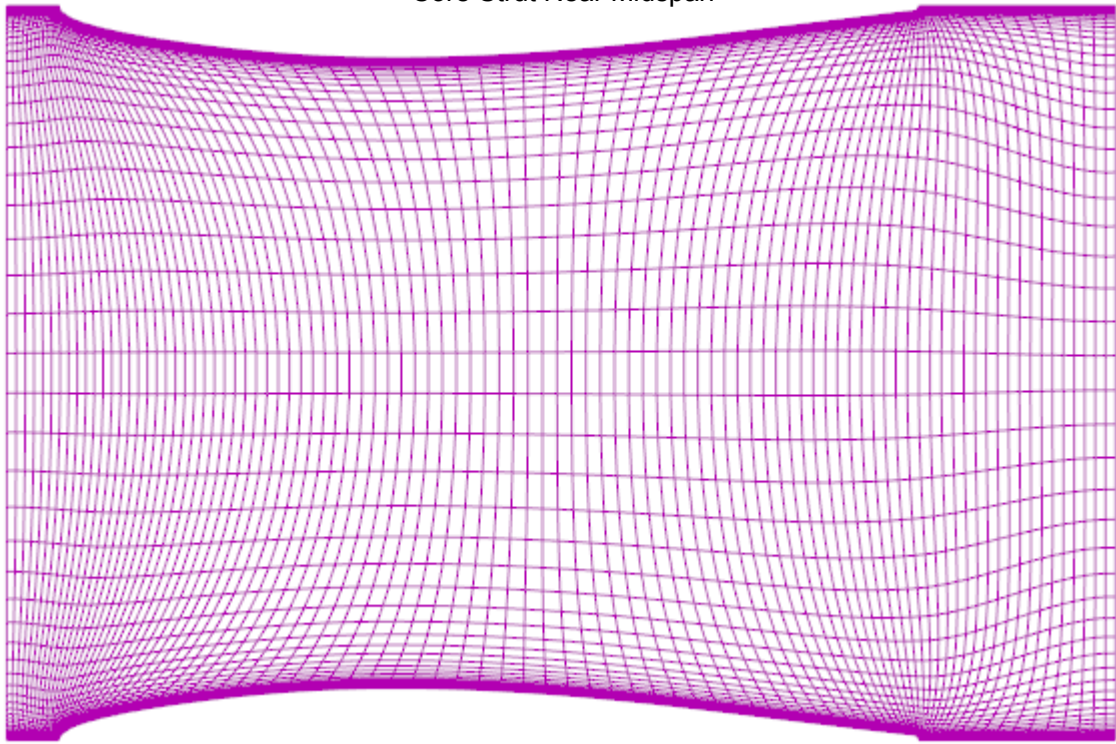
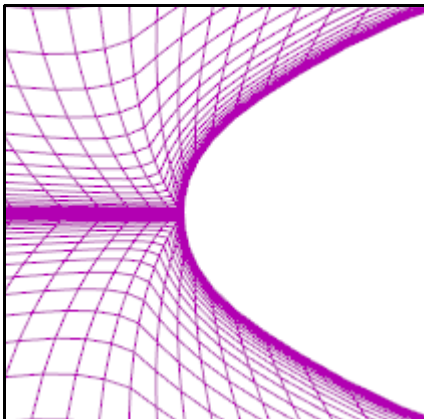


Figure 15: FEGV Grid at Block Downstream Boundaries

Core Strut Near Midspan



Leading Edge



Trailing Edge

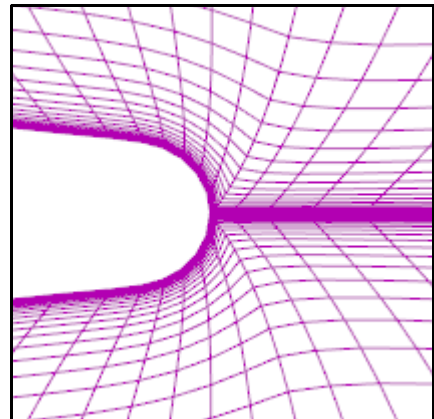


Figure 16: Core-Strut Grid at Near Midspan Location

Bypass-Strut and Core-Strut H-Grid
Downstream Boundaries

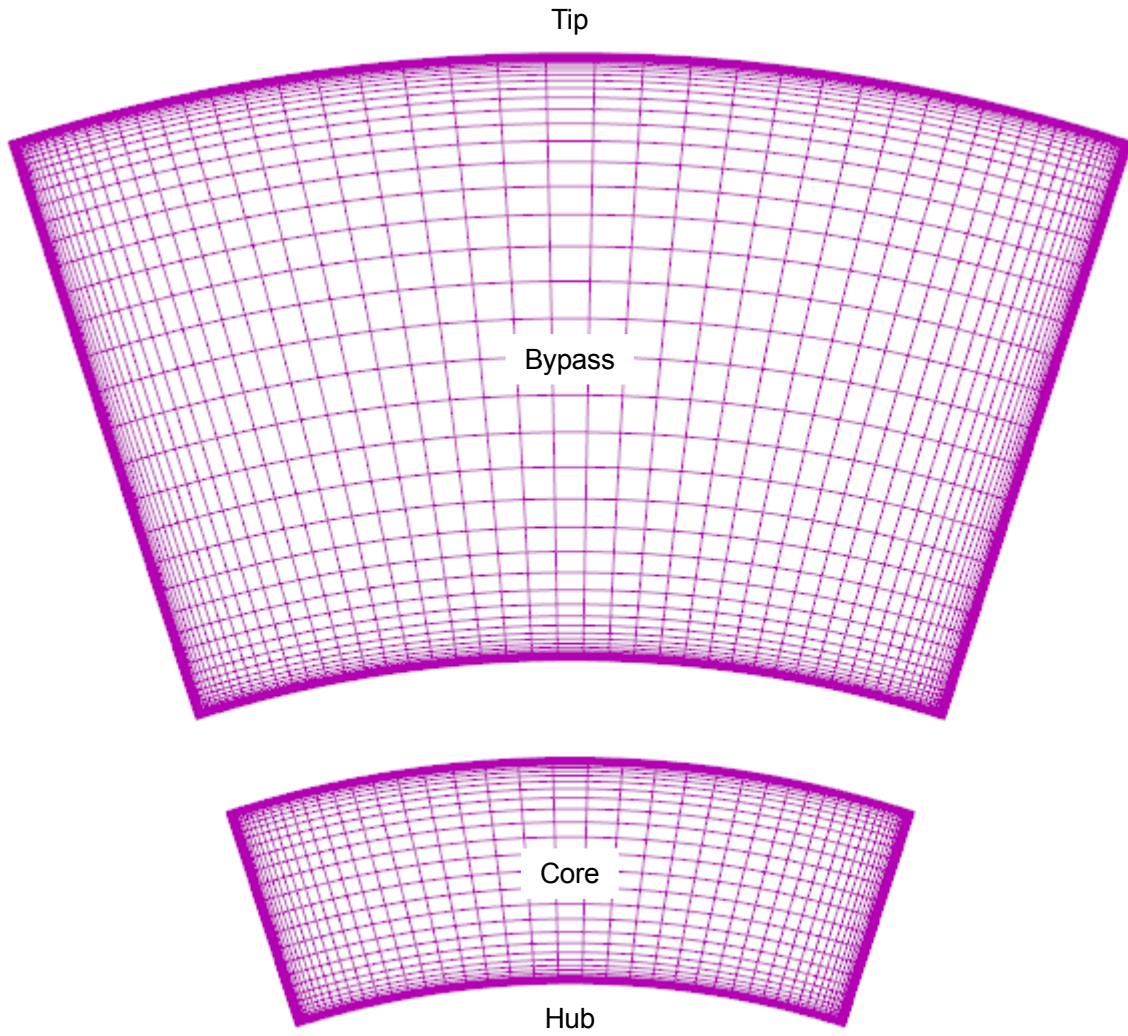


Figure 17: Bypass- and Core-Strut Grids at Block Downstream Boundaries

SLTO Operating Point

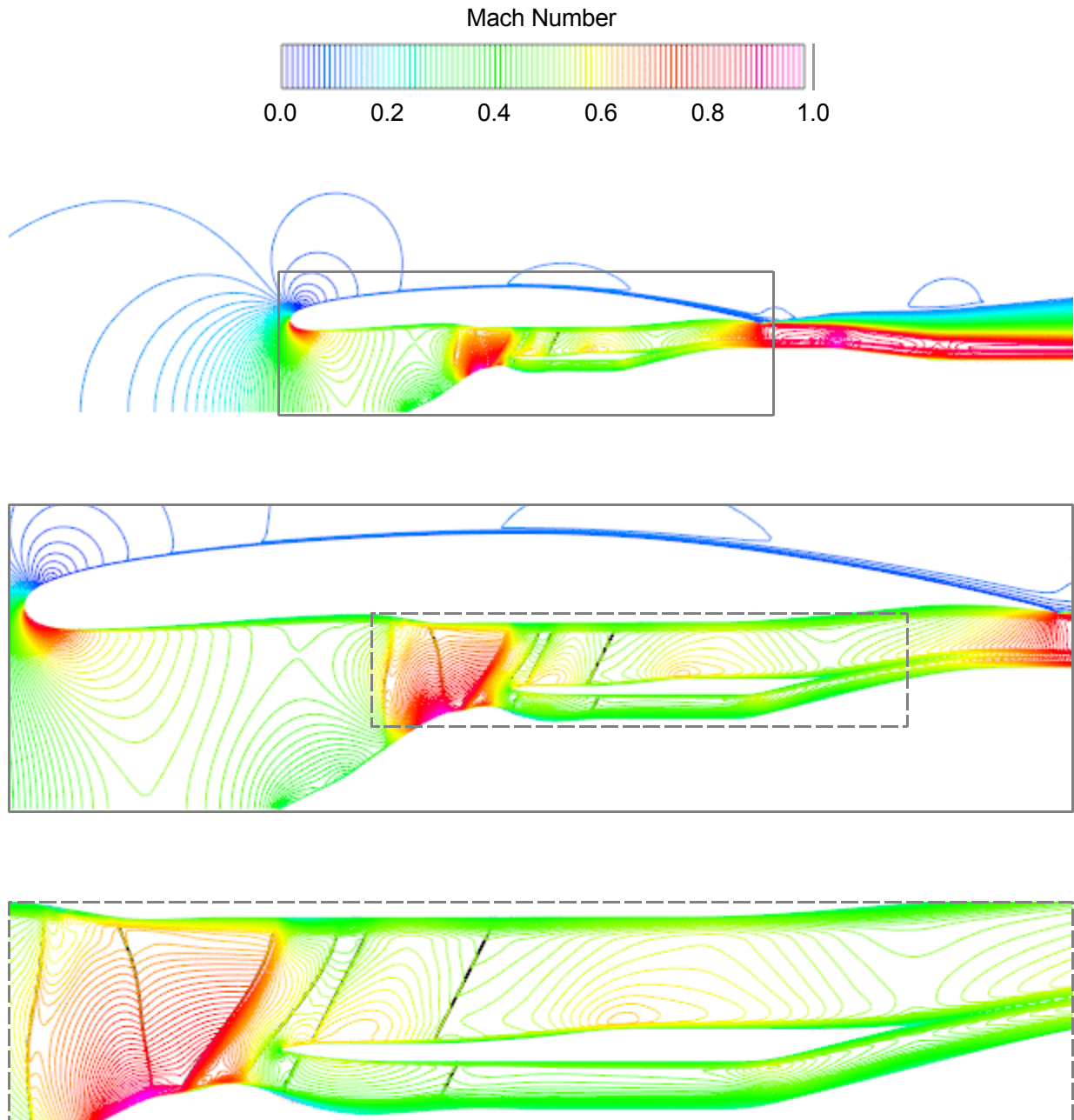


Figure 18: Computed Fan System Flow Field for the SLTO Operating Point; Pitchwise-Averaged Flow; Mach Number Contours

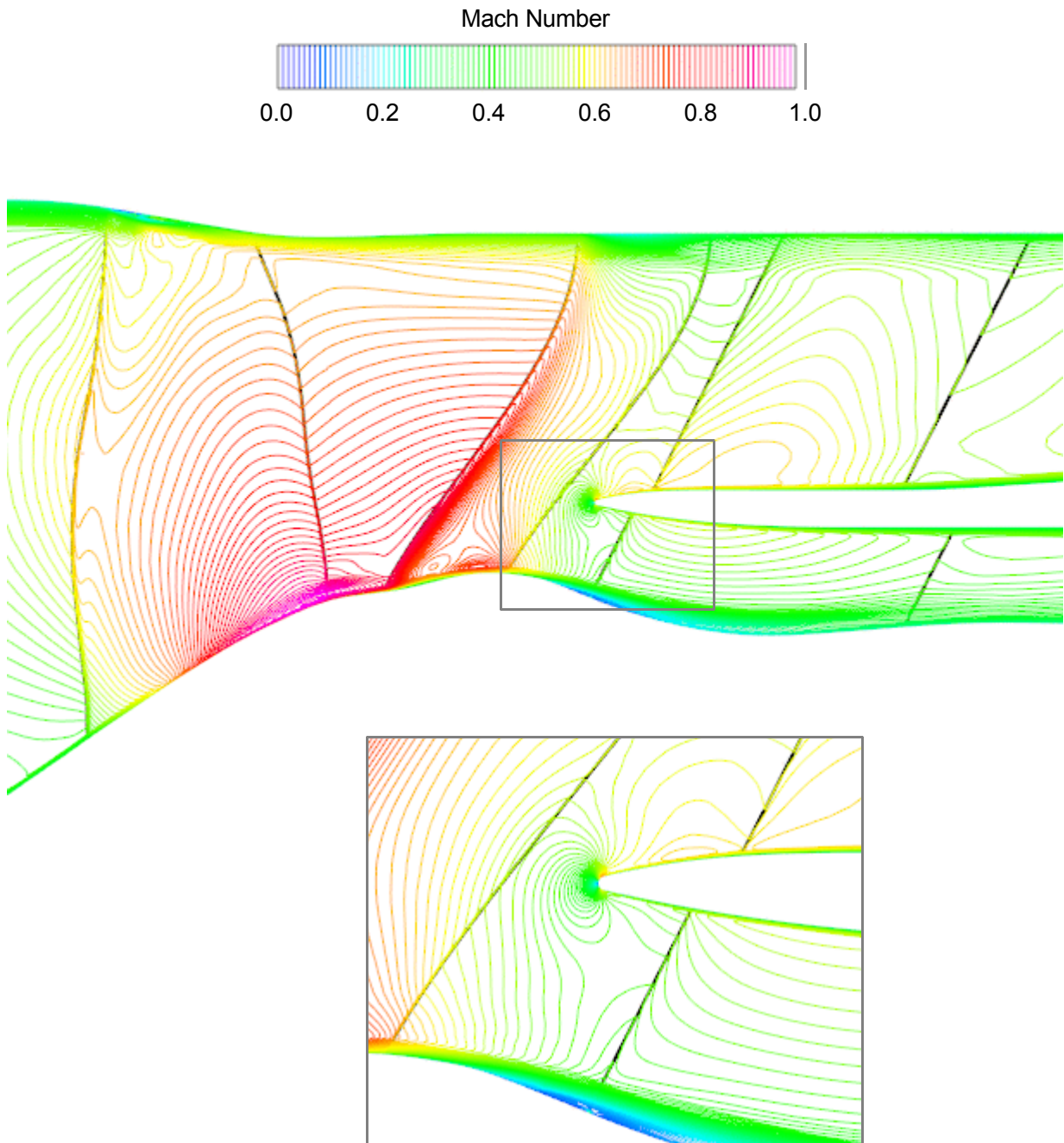


Figure 19: Computed Fan Blade Row Flow Fields for the SLTO Operating Point; Pitchwise-Averaged Flow; Mach Number Contours

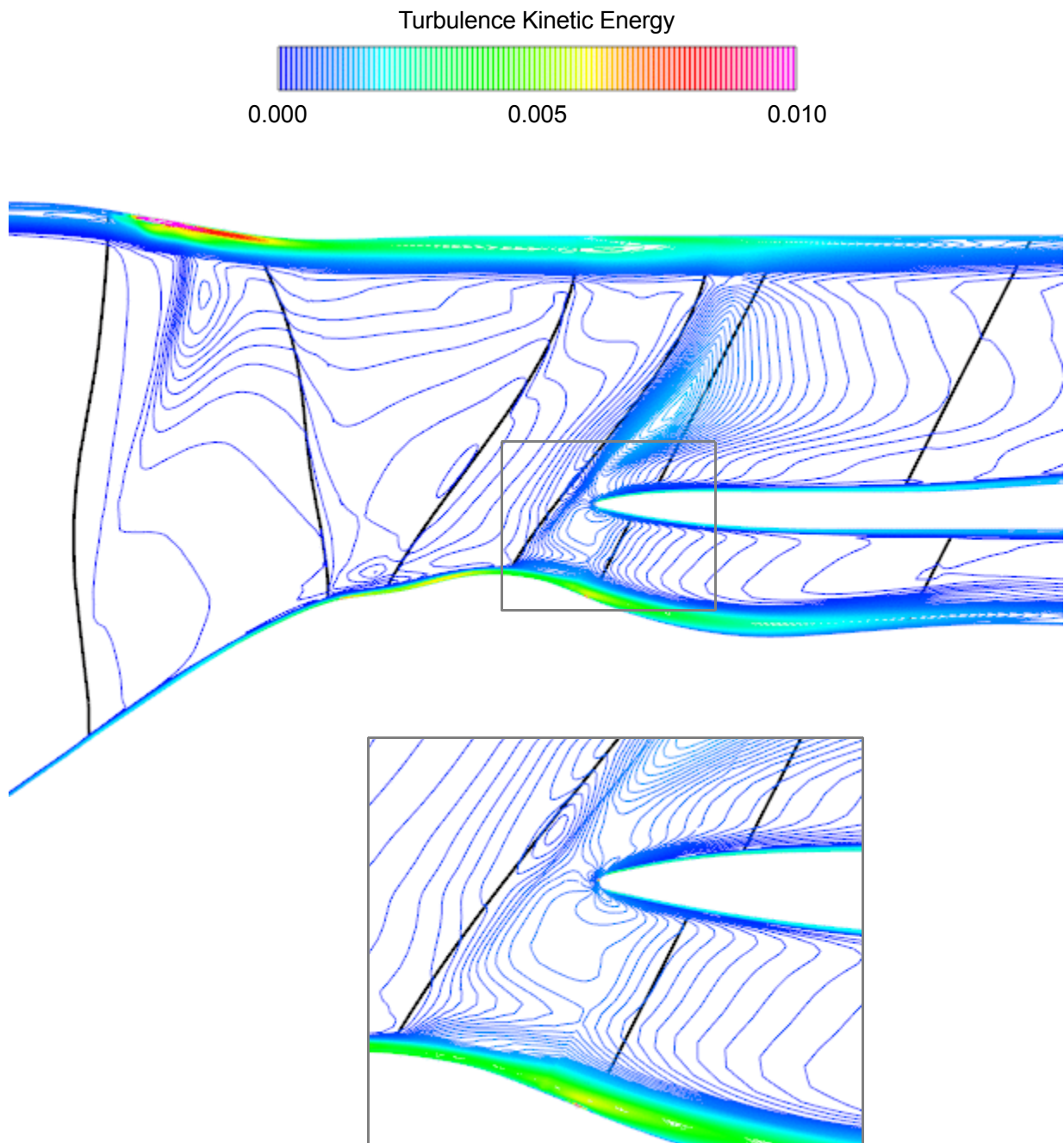


Figure 20: Computed Fan Blade Row Flow Fields for the SLTO Operating Point; Pitchwise-Averaged Flow; Turbulence Kinetic Energy Contours

SLTO Operating Point

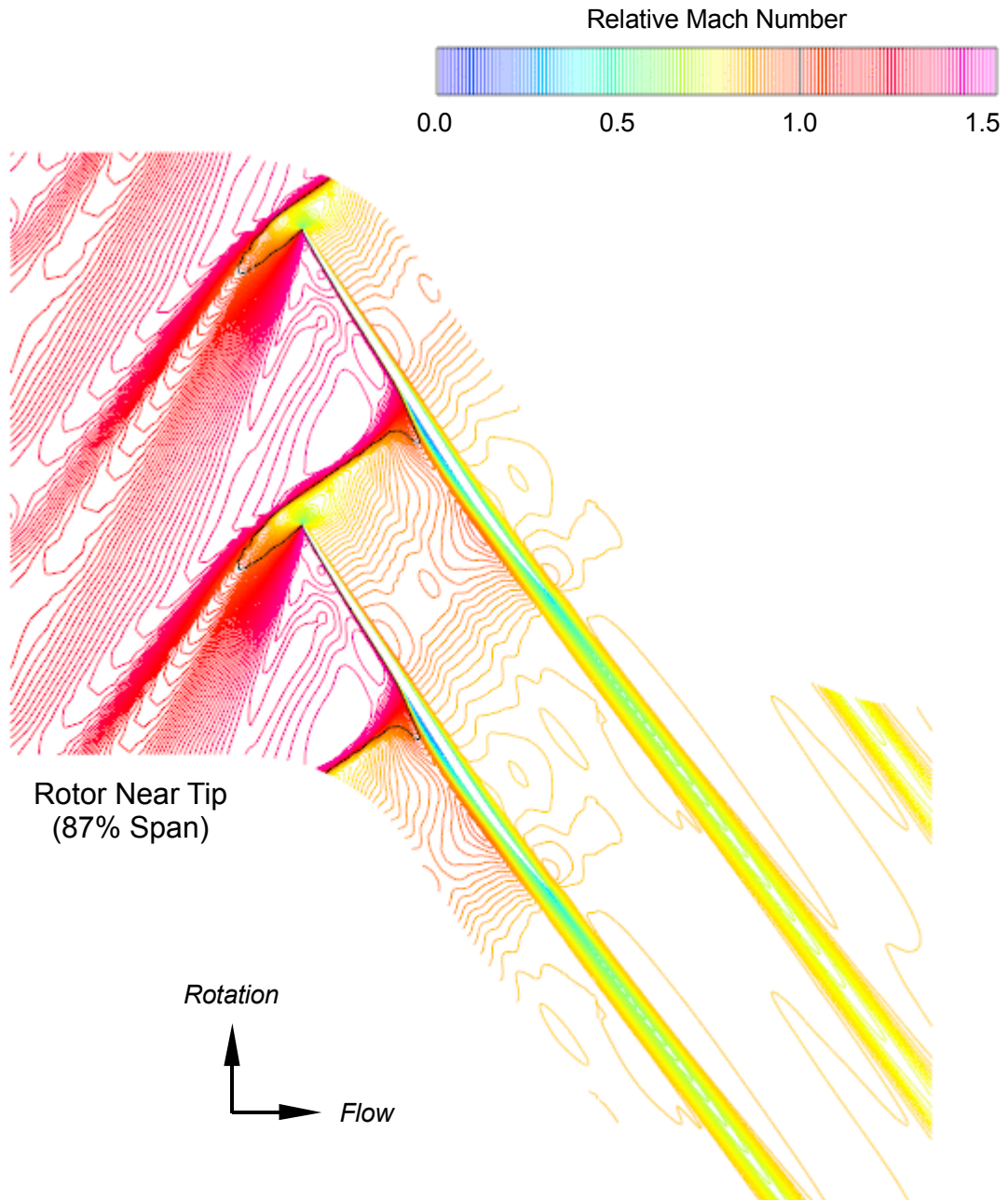
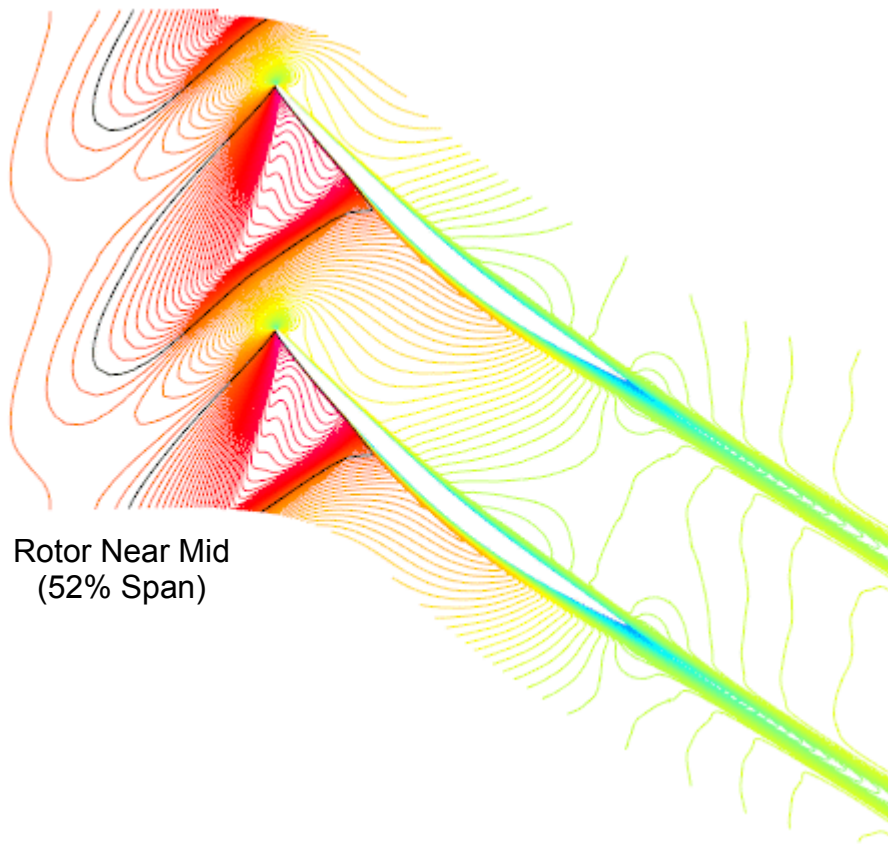
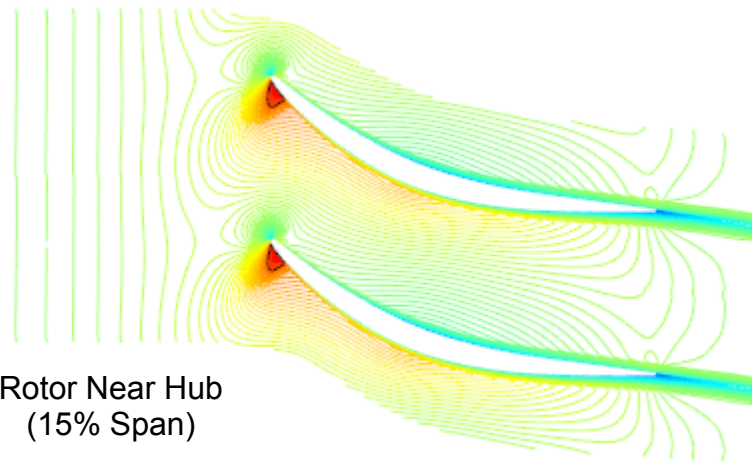


Figure 21a: Computed Rotor Flow Field for the SLTO Operating Point; Blade-to-Blade Relative Mach Number Contours



Rotor Near Mid
(52% Span)

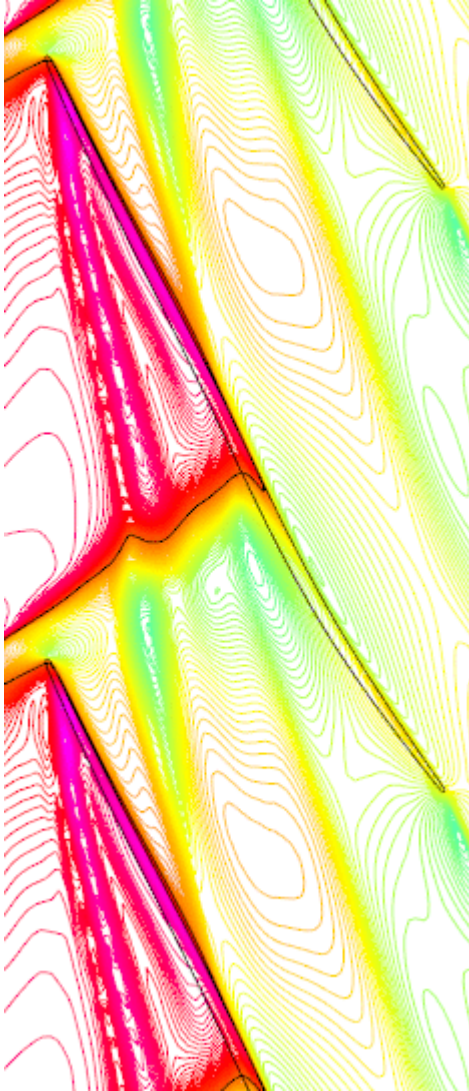


Rotor Near Hub
(15% Span)

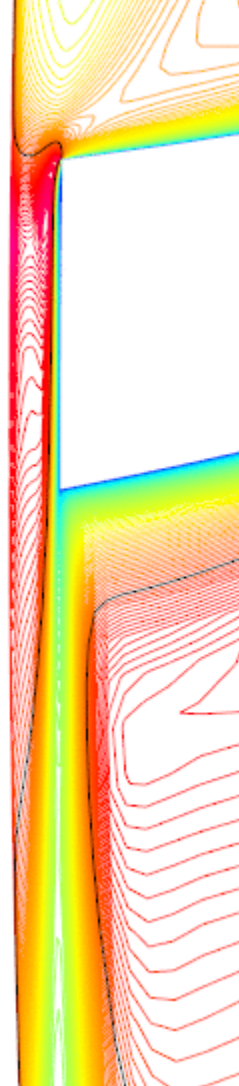
*Figure 21b: Computed Rotor Flow Field for the SLTO Operating Point;
Blade-to-Blade Relative Mach Number Contours*

Rotor Tip Clearance

Mid-Clearance-Gap
Spanwise Location



Mid-Chord
Axial Location



Rotation



Figure 22: Computed Rotor Tip Flow Field for the SLTO Operating Point; Relative Mach Number Contours (Legend in Figure 21a)

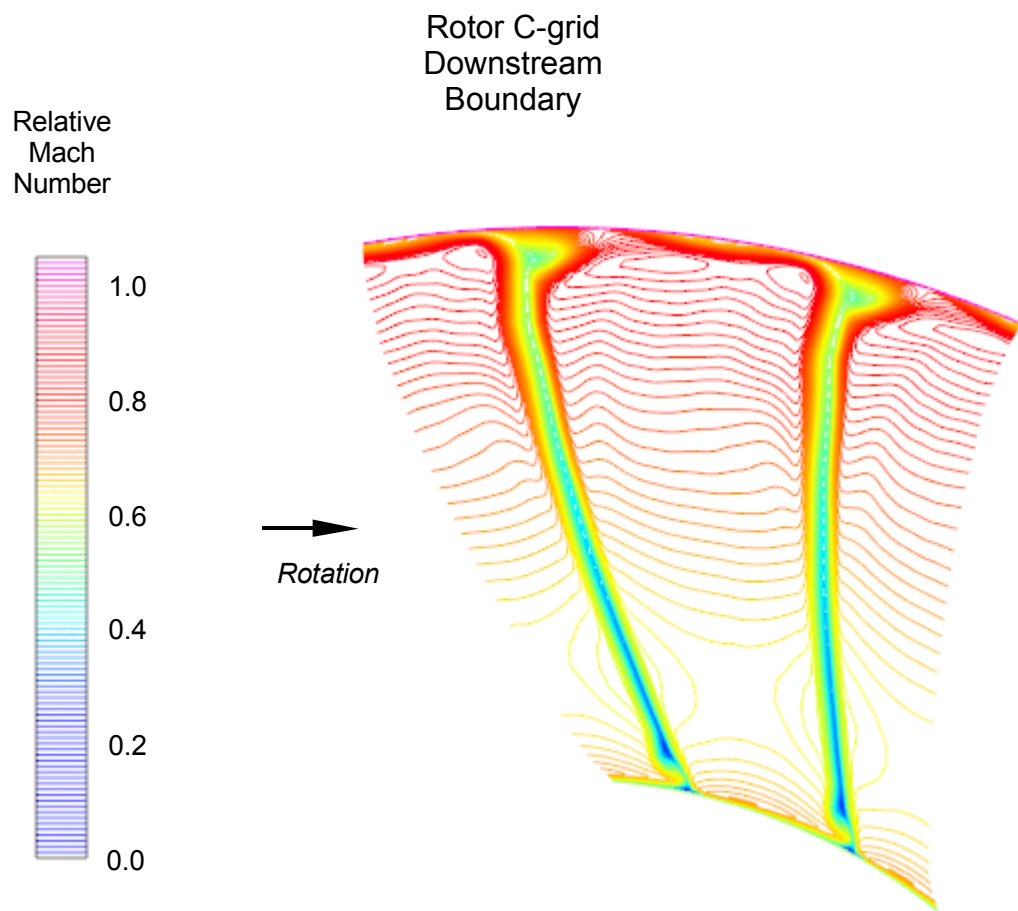


Figure 23: Computed Rotor Flow Field for the SLTO Operating Point; Downstream Boundary of C-Grid; Relative Mach Number Contours

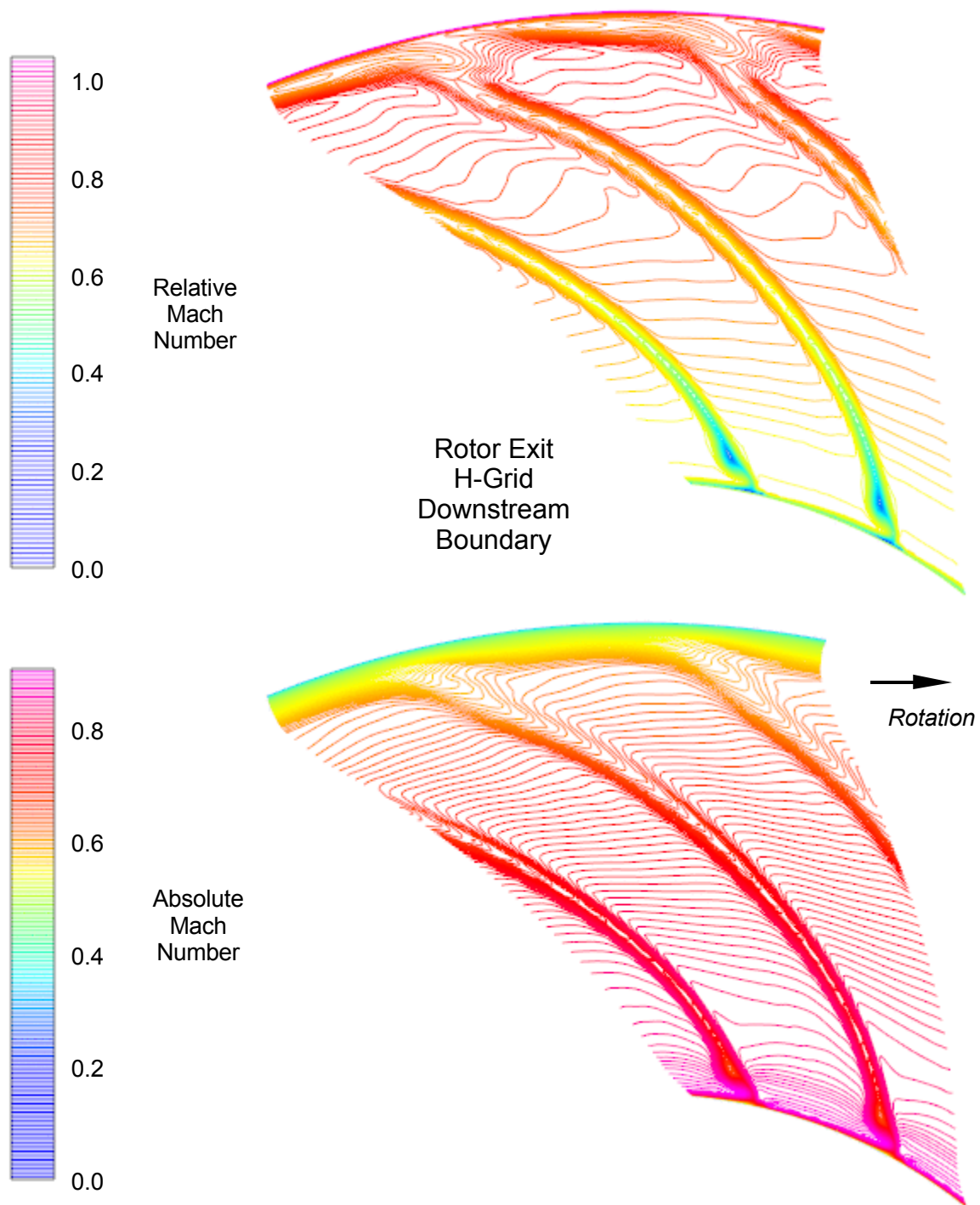


Figure 24a: Computed Rotor Flow Field for the SLTO Operating Point; Downstream Mixing Plane; Relative and Absolute Mach Number Contours

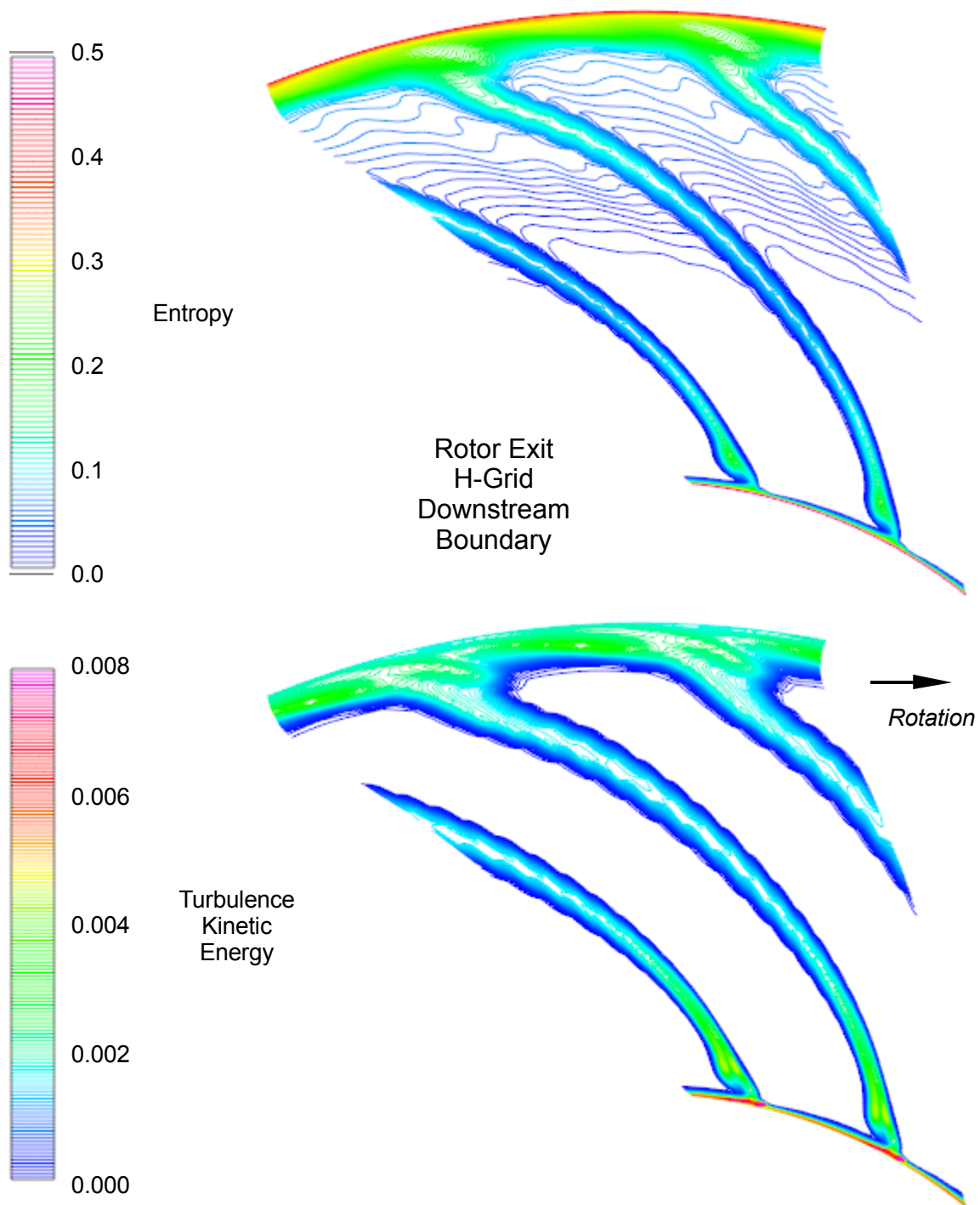
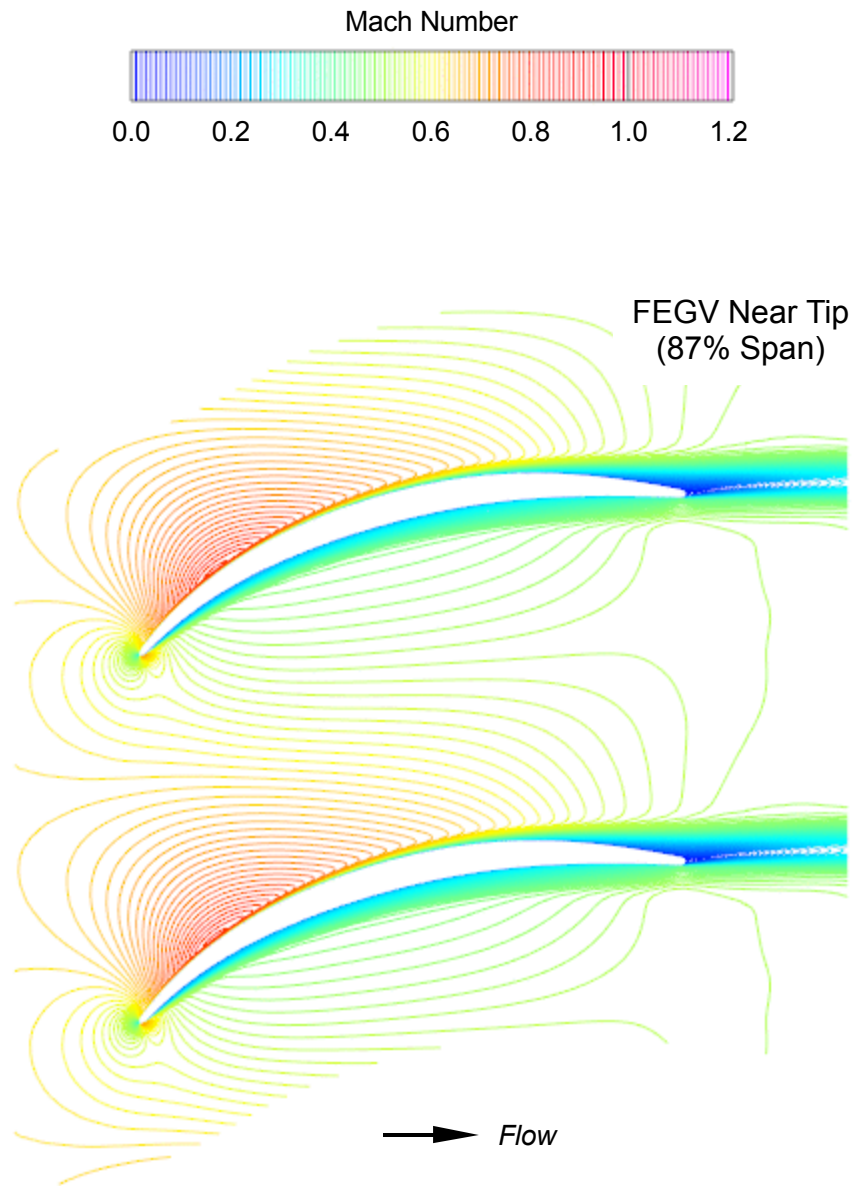
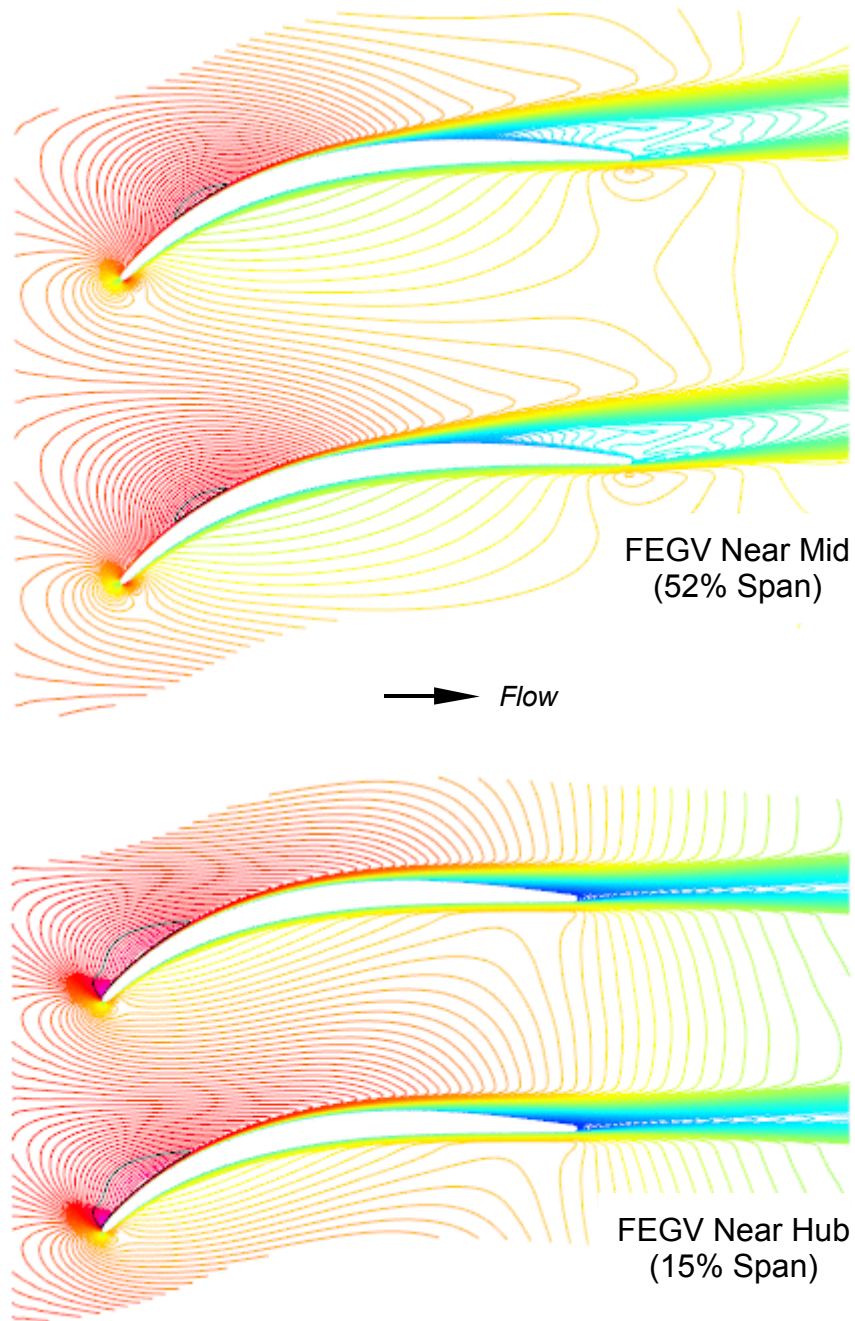


Figure 24b: Computed Rotor Flow Field for the SLTO Operating Point; Downstream Mixing Plane; Entropy and Turbulence Kinetic Energy Contours

SLTO Operating Point



*Figure 25a: Computed FEGV Flow Field for the SLTO Operating Point;
Blade-to-Blade Mach Number Contours*



*Figure 25b: Computed FEGV Flow Field for the SLTO Operating Point;
Blade-to-Blade Mach Number Contours*

FEGV C-Grid
Downstream
Boundary

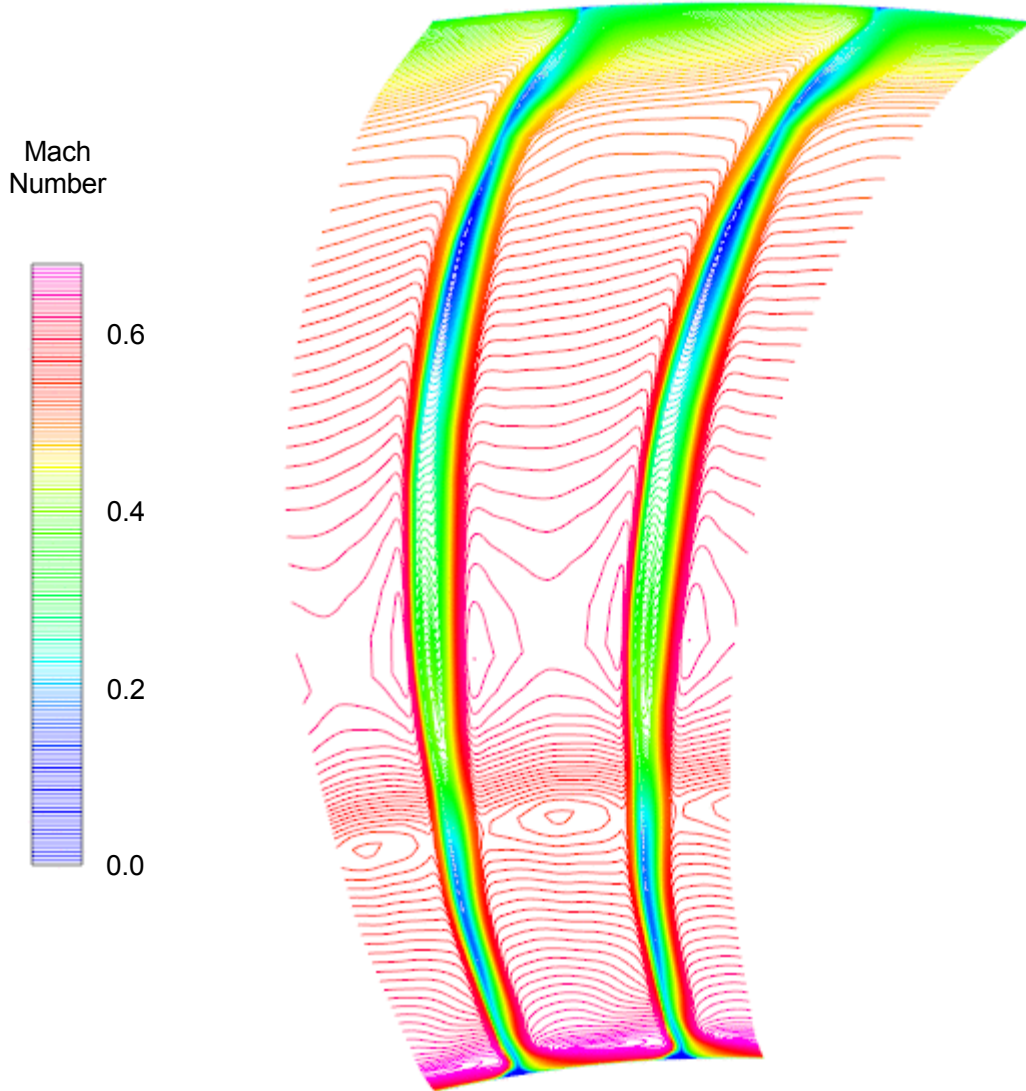


Figure 26: Computed FEGV Flow Field for the SLTO Operating Point; Downstream Boundary of C-Grid; Mach Number Contours

FEGV Exit
H-Grid
Downstream
Boundary

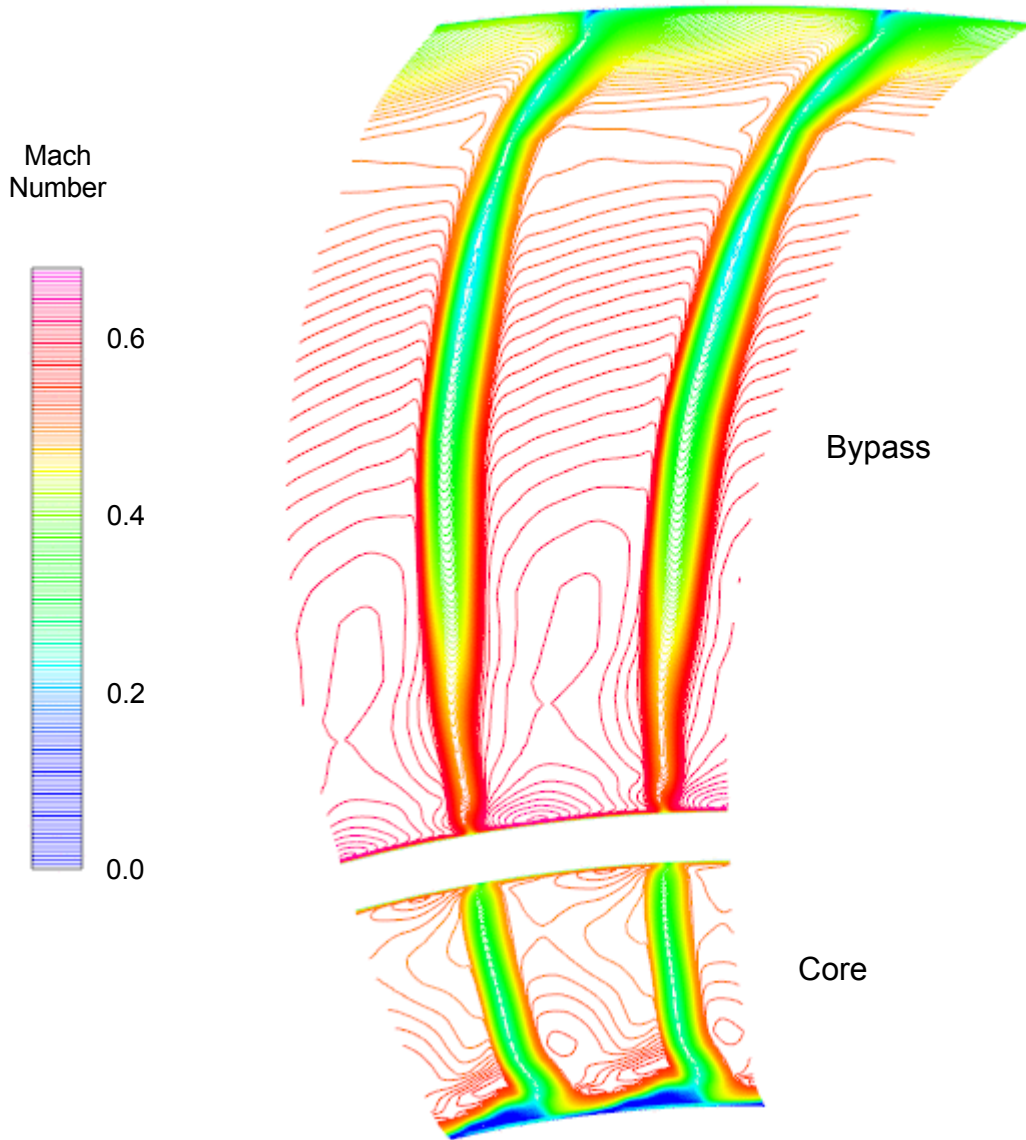
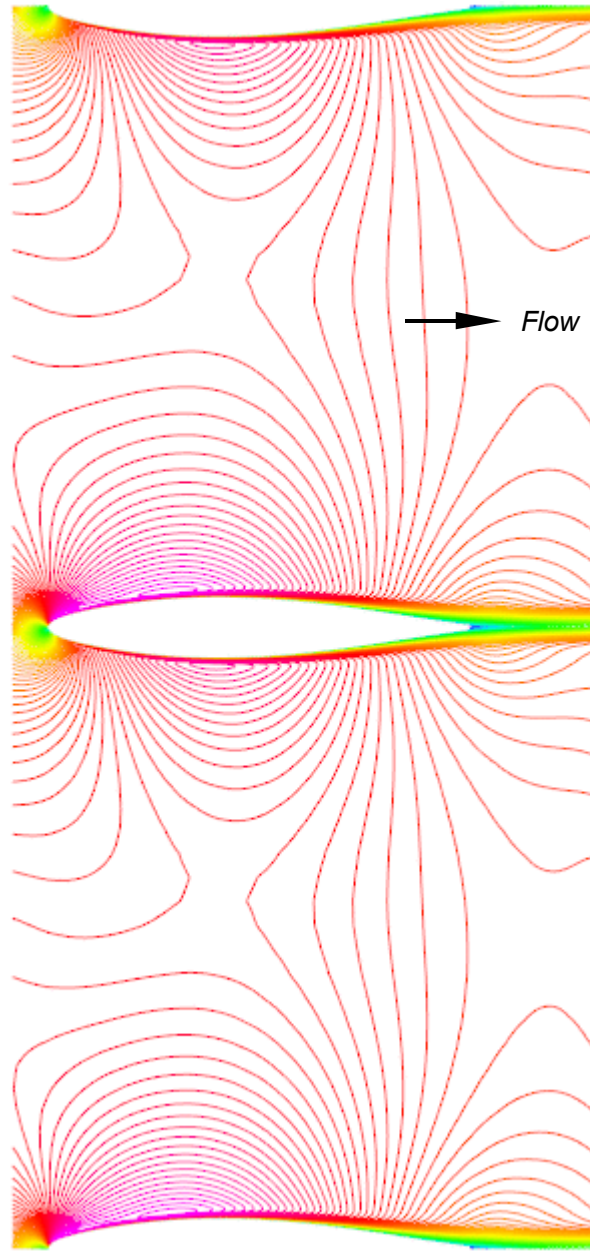
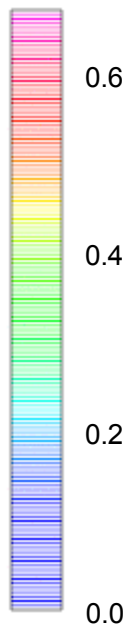


Figure 27: Computed FEGV Flow Field for the SLTO Operating Point; Downstream Mixing Planes; Mach Number Contours

SLTO Operating Point

Bypass Strut
Near Midspan

Mach
Number



*Figure 28: Computed Bypass Strut Flow Field for the SLTO Operating Point;
Blade-to-Blade Mach Number Contours*

Bypass-Strut and Core-Strut H-Grid
Downstream Boundaries

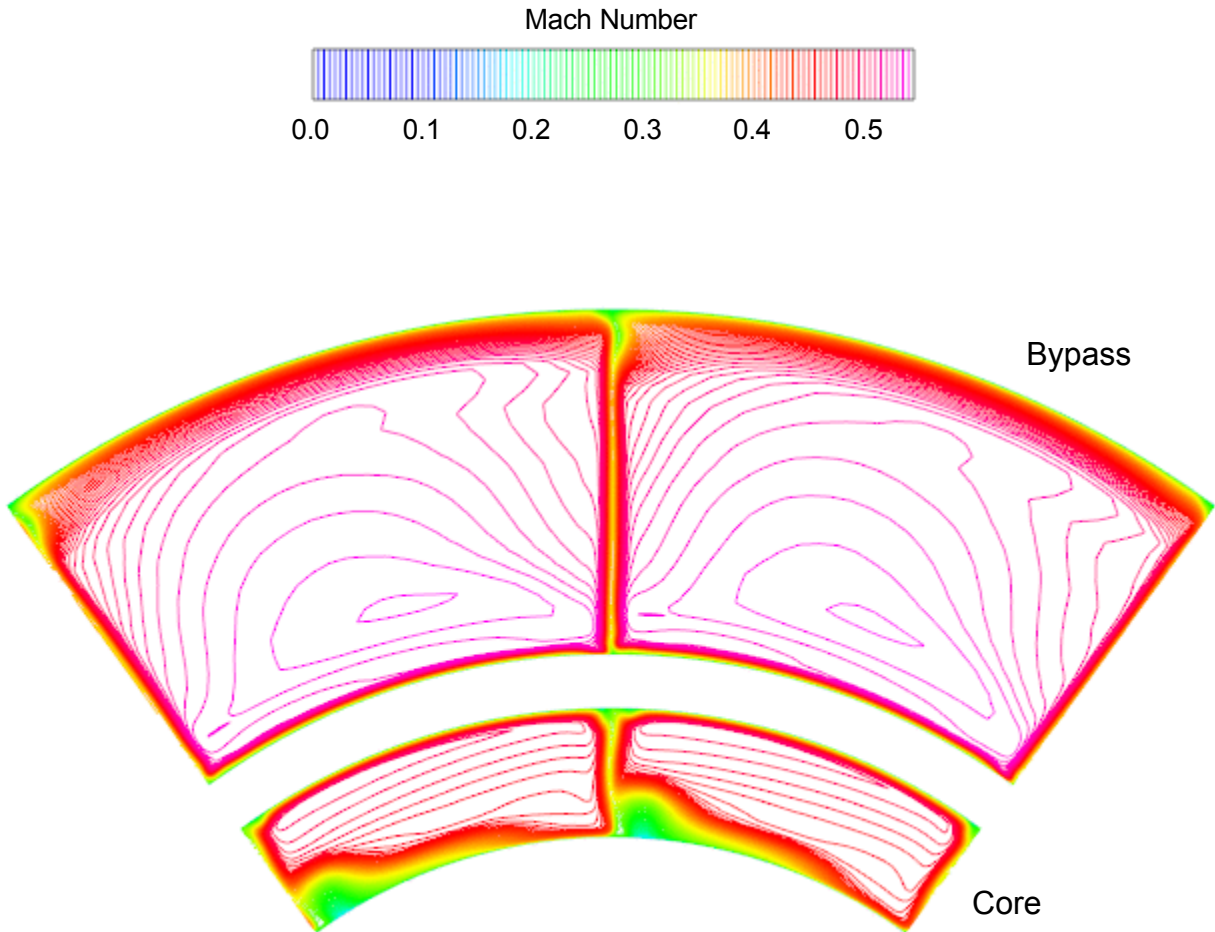


Figure 29: Computed Bypass and Core Strut Flow Fields for the SLTO Operating Point; Downstream Mixing Planes; Mach Number Contours

Cutback Operating Point

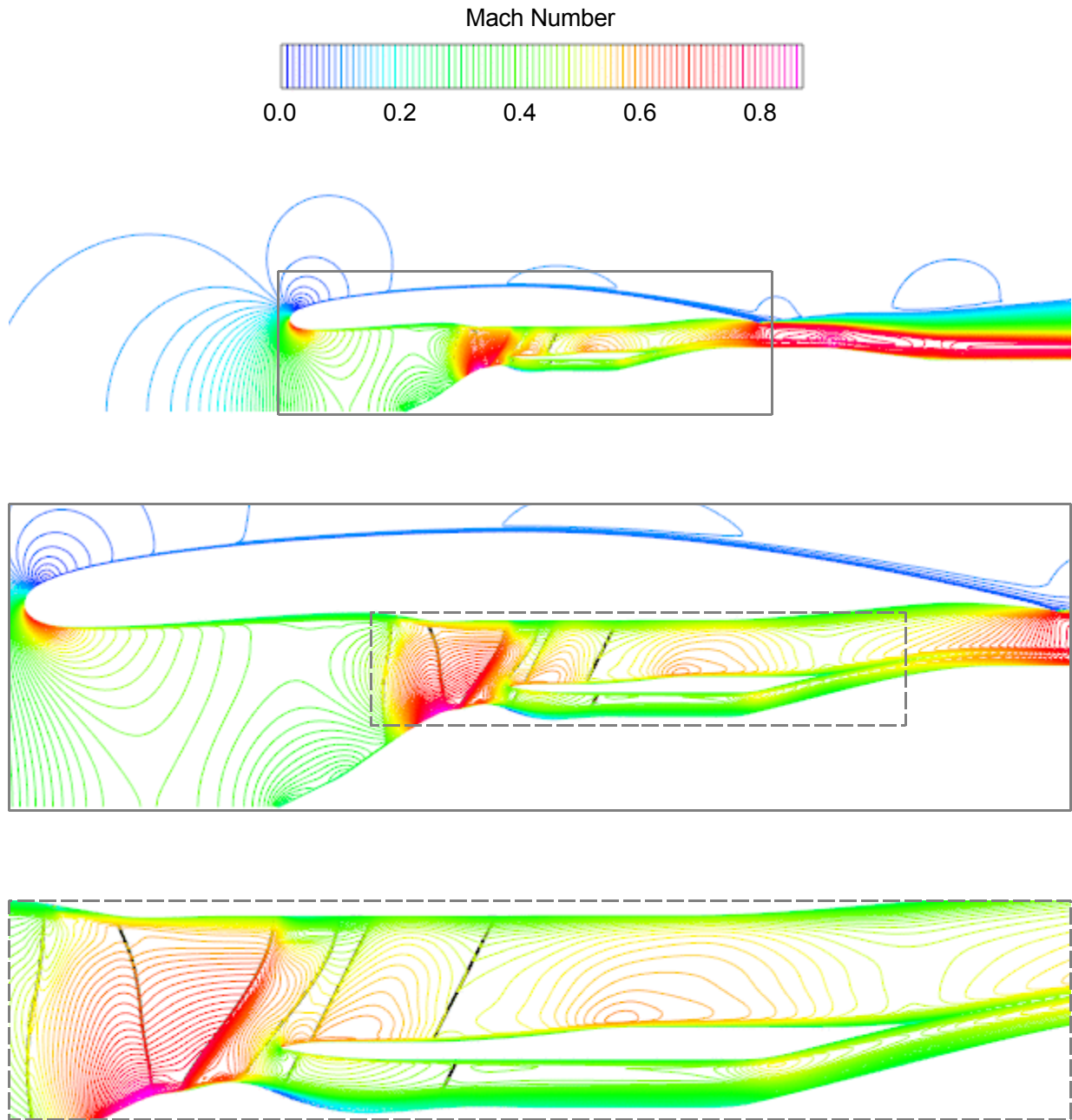


Figure 30: Computed Fan System Flow Field for the Cutback Operating Point; Pitchwise-Averaged Flow; Mach Number Contours

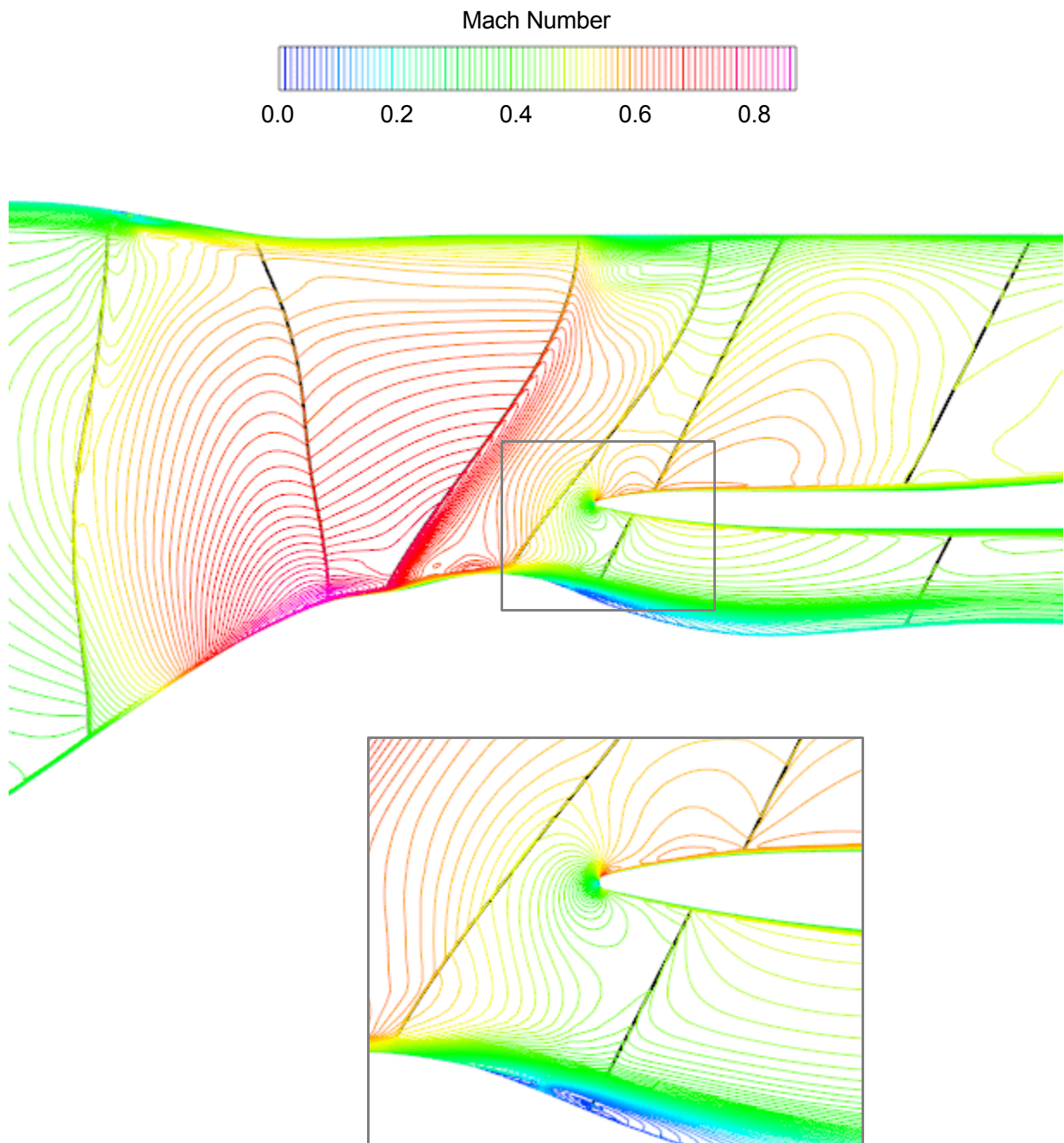


Figure 31: Computed Fan Blade Row Flow Fields for the Cutback Operating Point; Pitchwise-Averaged Flow; Mach Number Contours

Cutback Operating Point

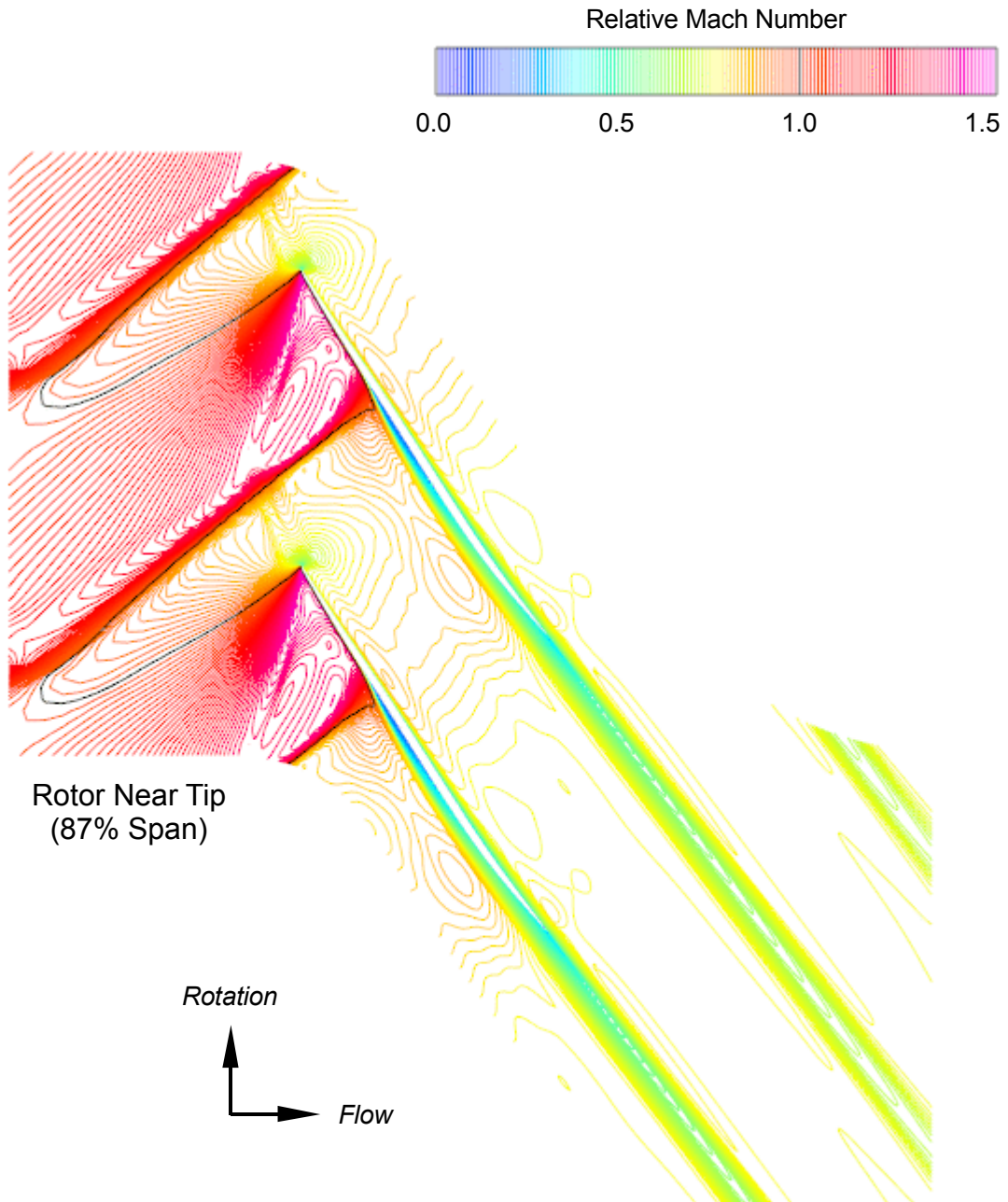
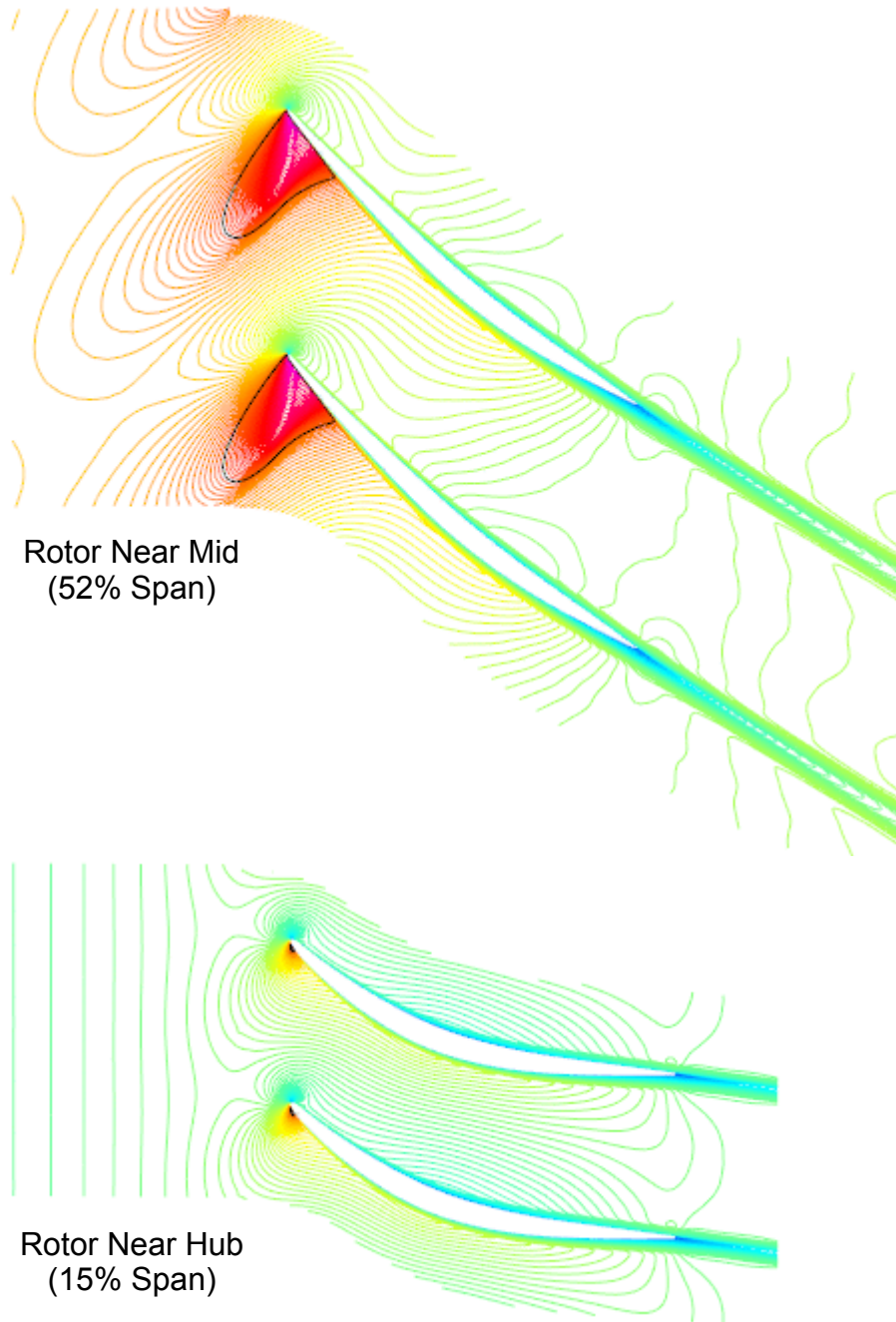


Figure 32a: Computed Rotor Flow Field for the Cutback Operating Point;
Blade-to-Blade Relative Mach Number Contours



*Figure 32b: Computed Rotor Flow Field for the Cutback Operating Point;
Blade-to-Blade Relative Mach Number Contours*

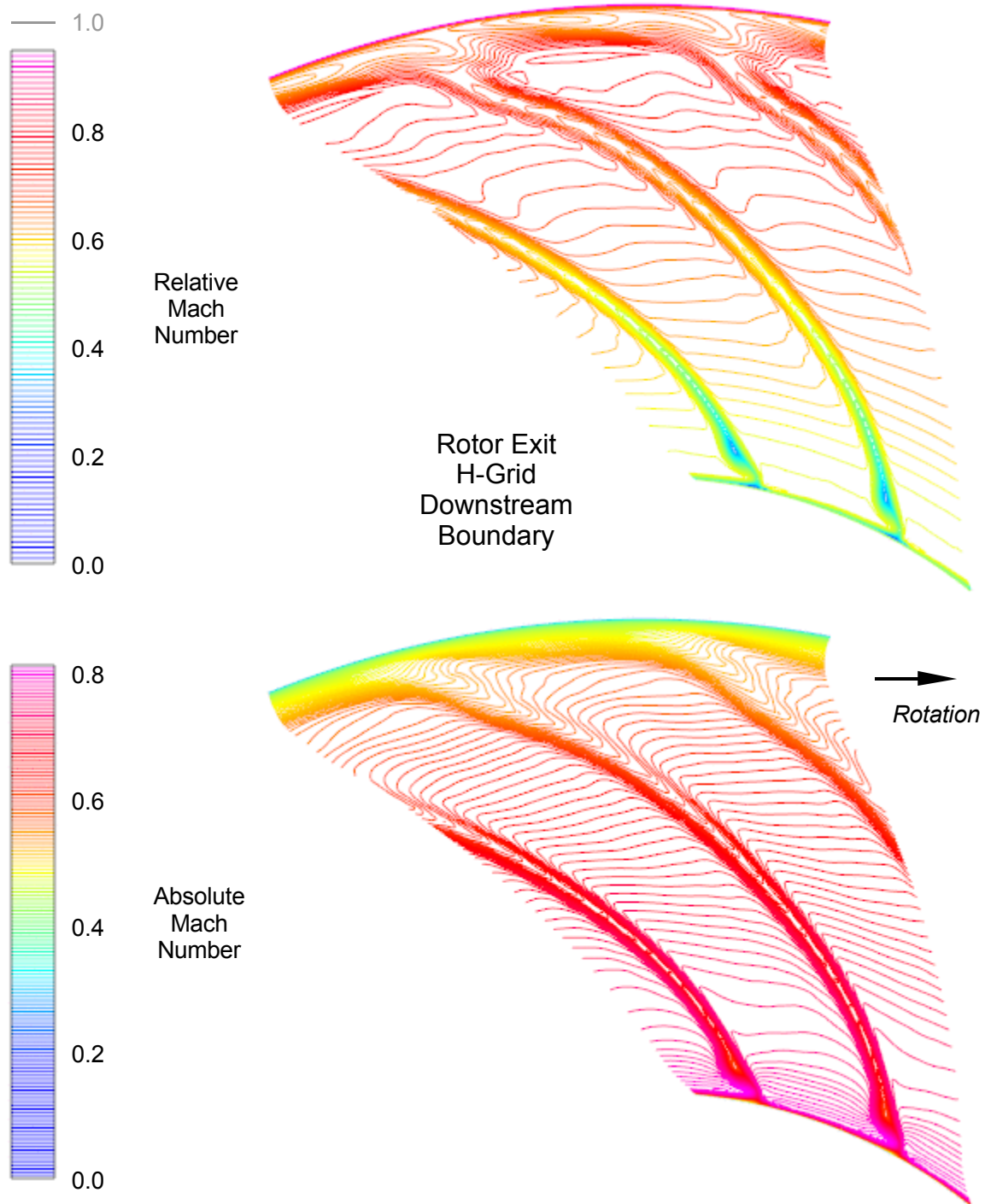


Figure 33a: Computed Rotor Flow Field for the Cutback Operating Point; Downstream Mixing Plane; Relative and Absolute Mach Number Contours

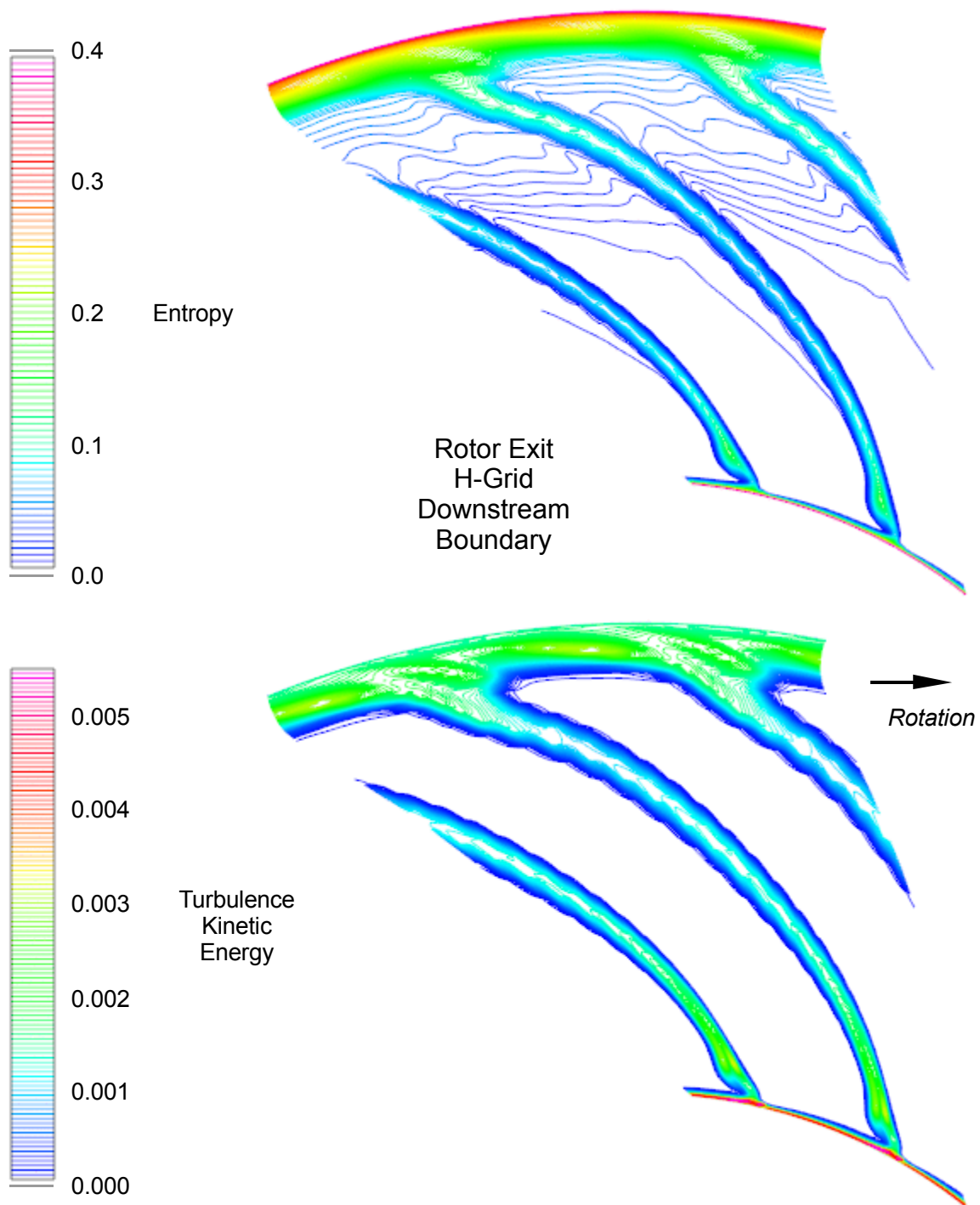


Figure 33b: Computed Rotor Flow Field for the Cutback Operating Point; Downstream Mixing Plane; Entropy and Turbulence Kinetic Energy Contours

Approach Operating Point

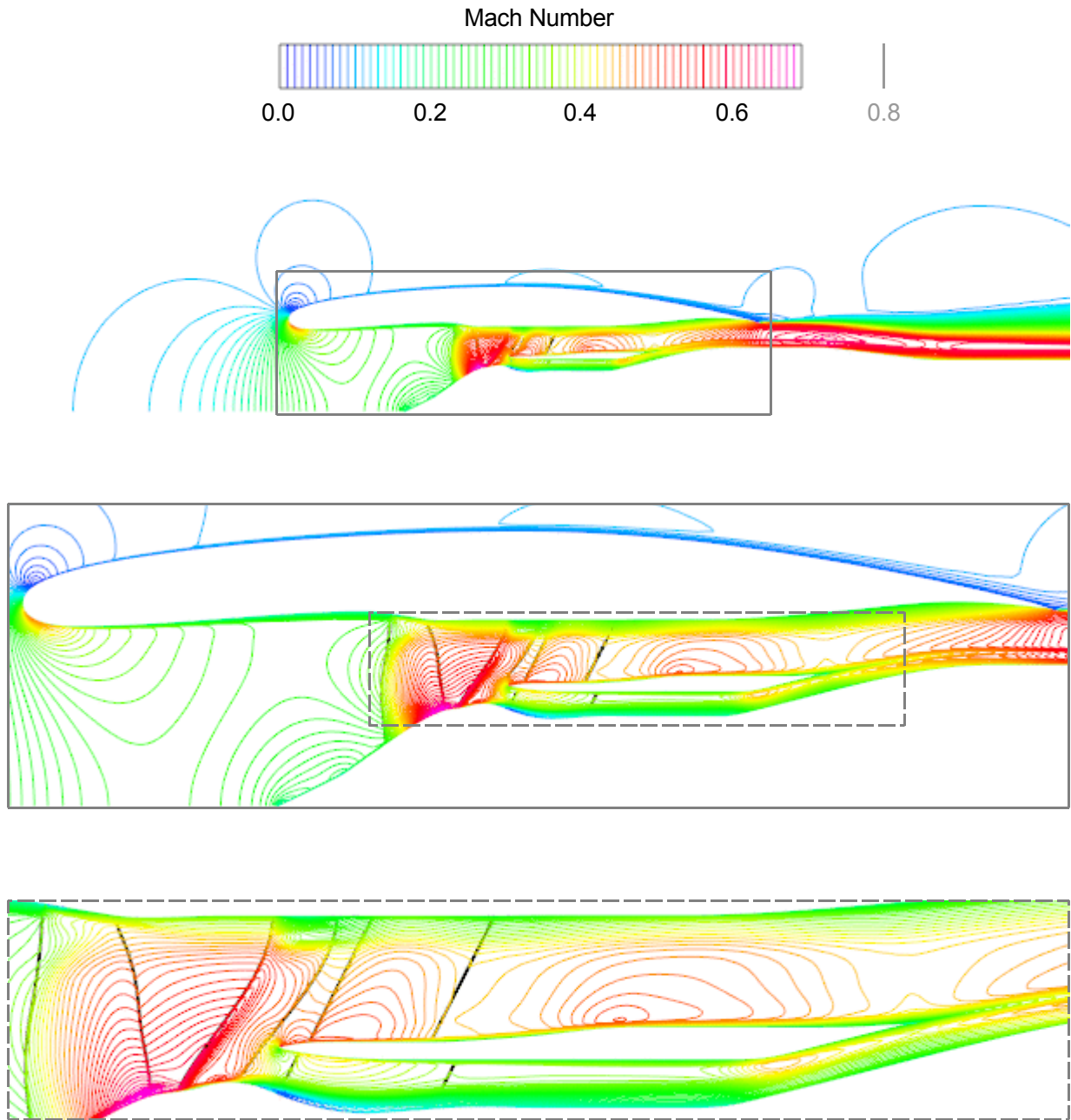


Figure 34: Computed Fan System Flow Field for the Approach Operating Point; Pitchwise-Averaged Flow; Mach Number Contours

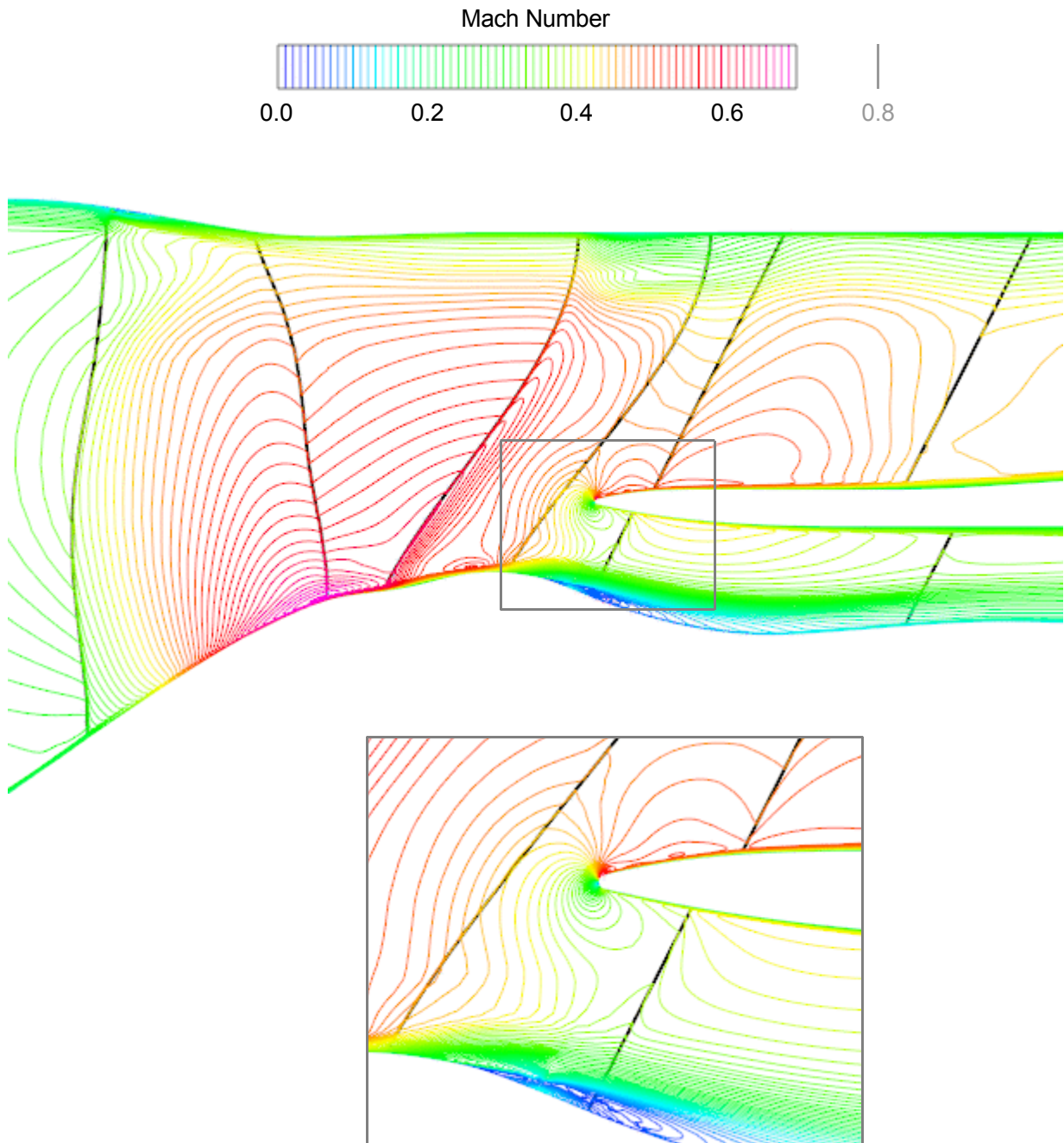


Figure 35: Computed Fan Blade Row Flow Fields for the Approach Operating Point; Pitchwise-Averaged Flow; Mach Number Contours

Approach Operating Point

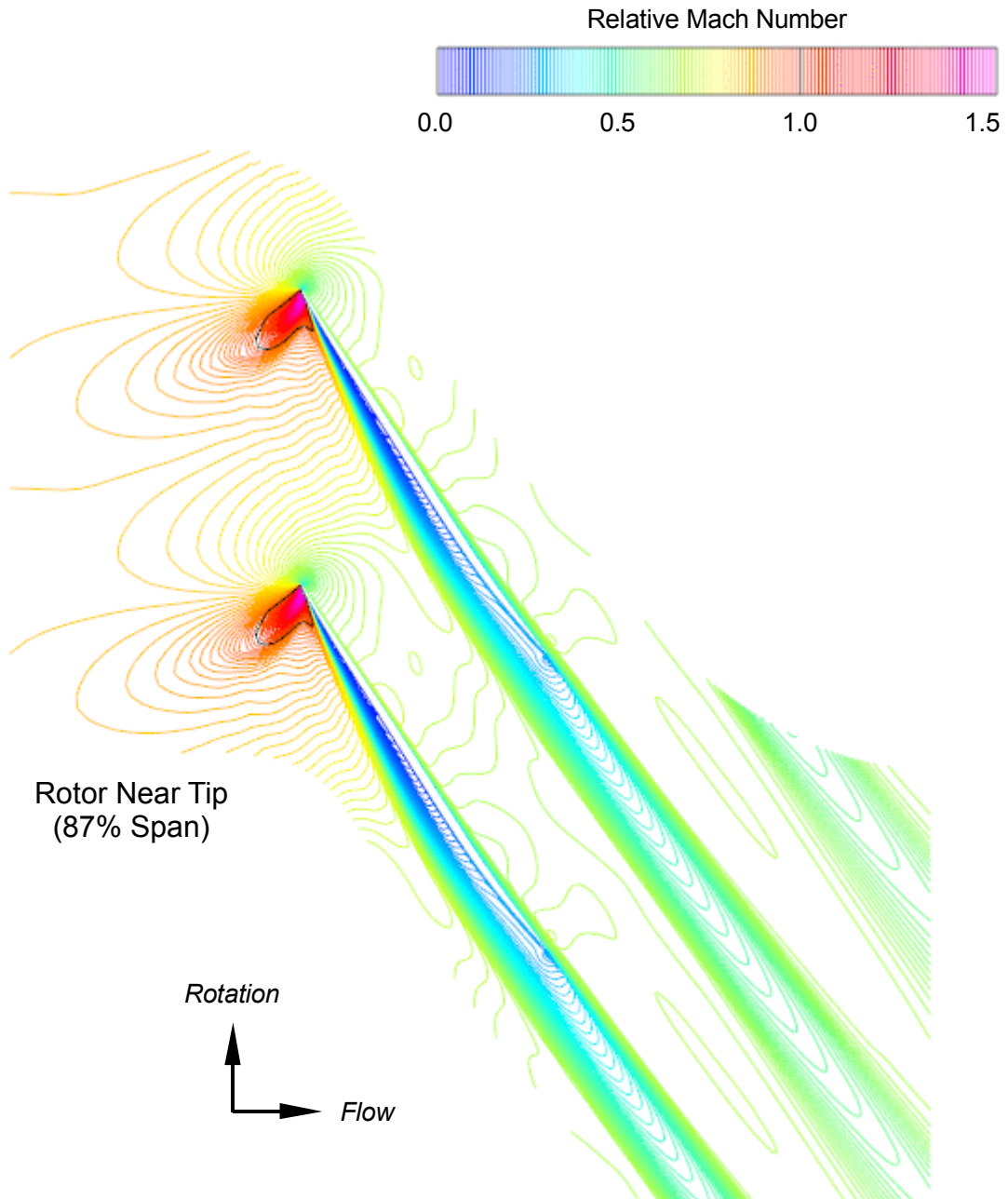
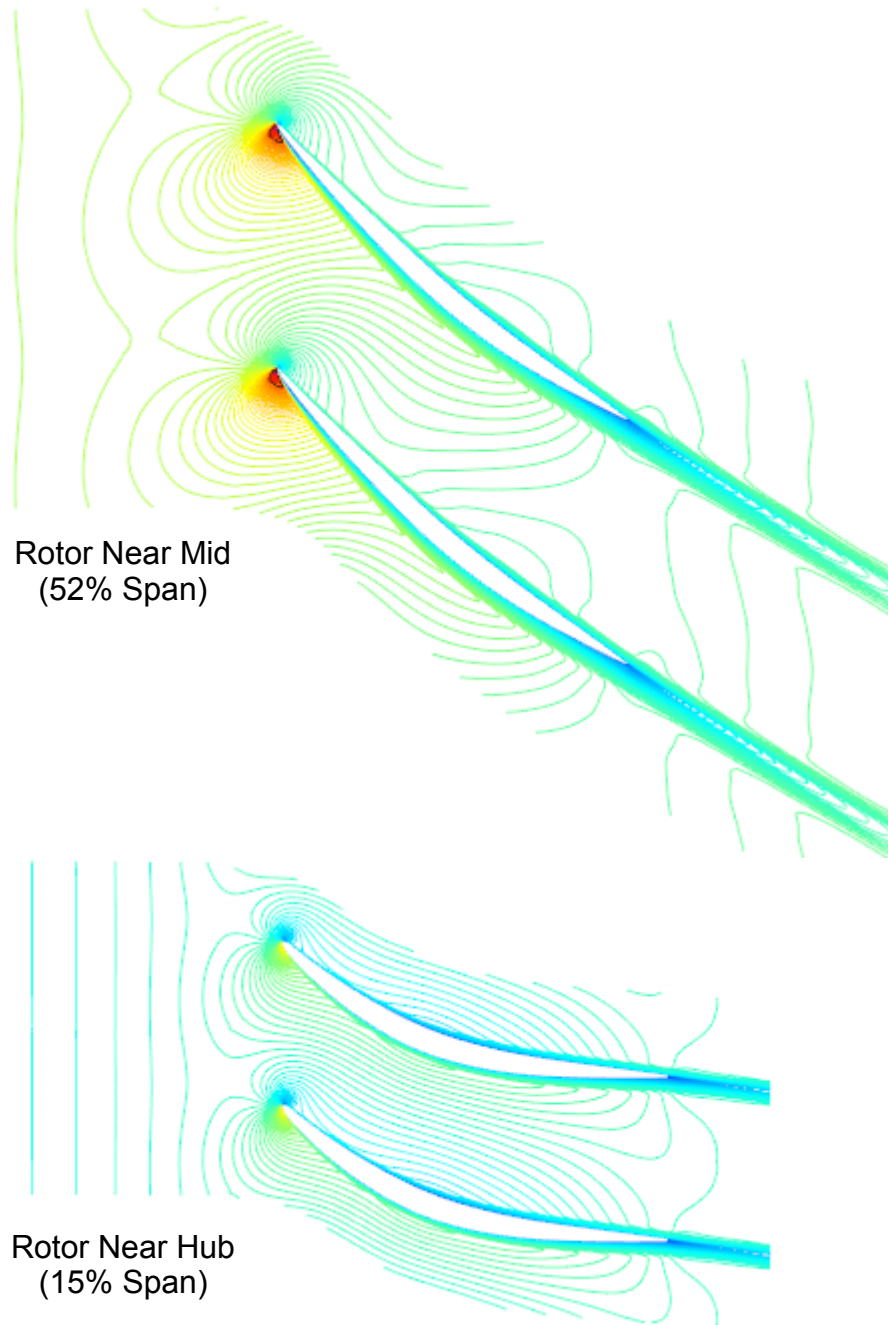


Figure 36a: Computed Rotor Flow Field for the Approach Operating Point; Blade-to-Blade Relative Mach Number Contours



*Figure 36b: Computed Rotor Flow Field for the Approach Operating Point;
Blade-to-Blade Relative Mach Number Contours*

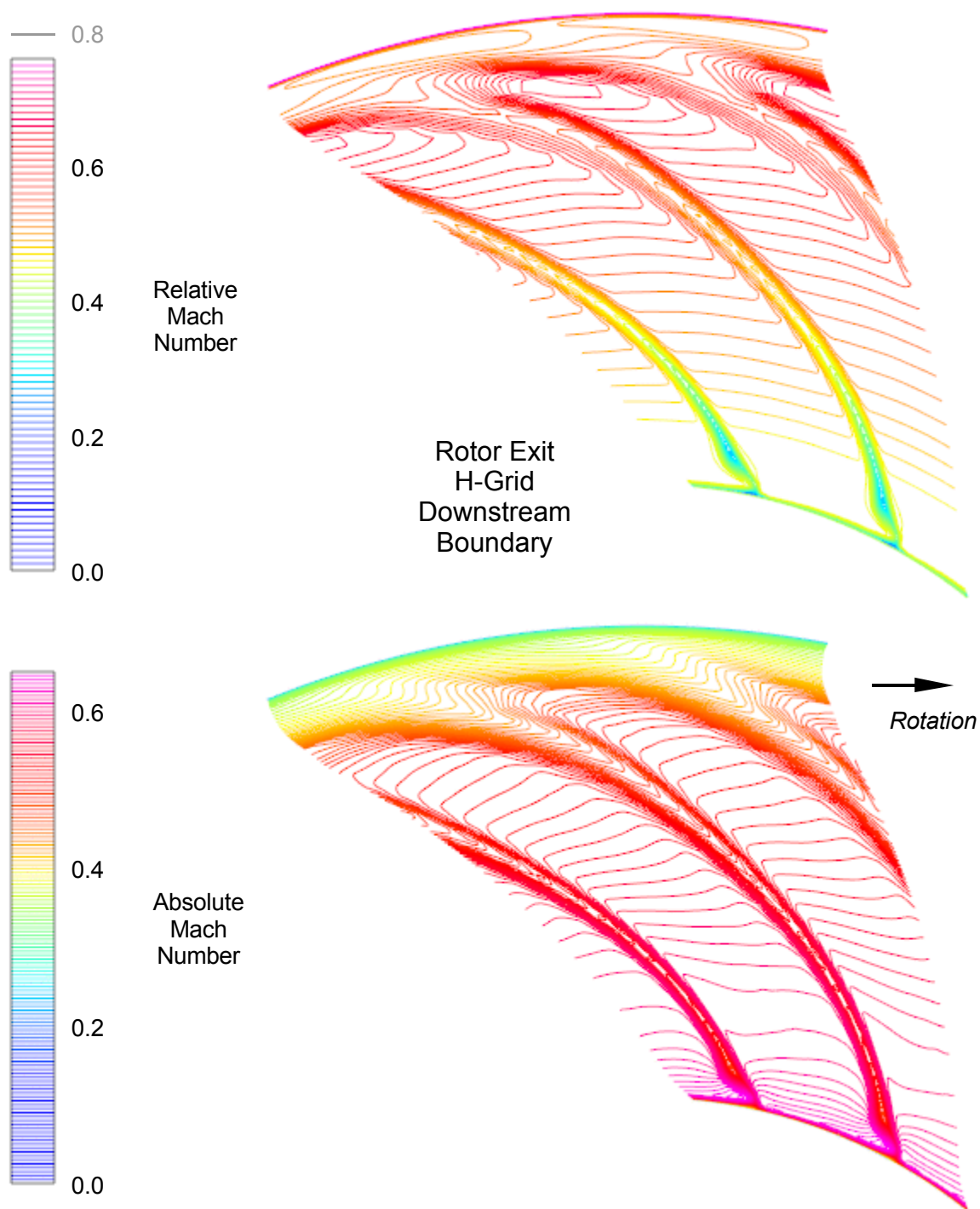


Figure 37a: Computed Rotor Flow Field for the Approach Operating Point; Downstream Mixing Plane; Relative and Absolute Mach Number Contours

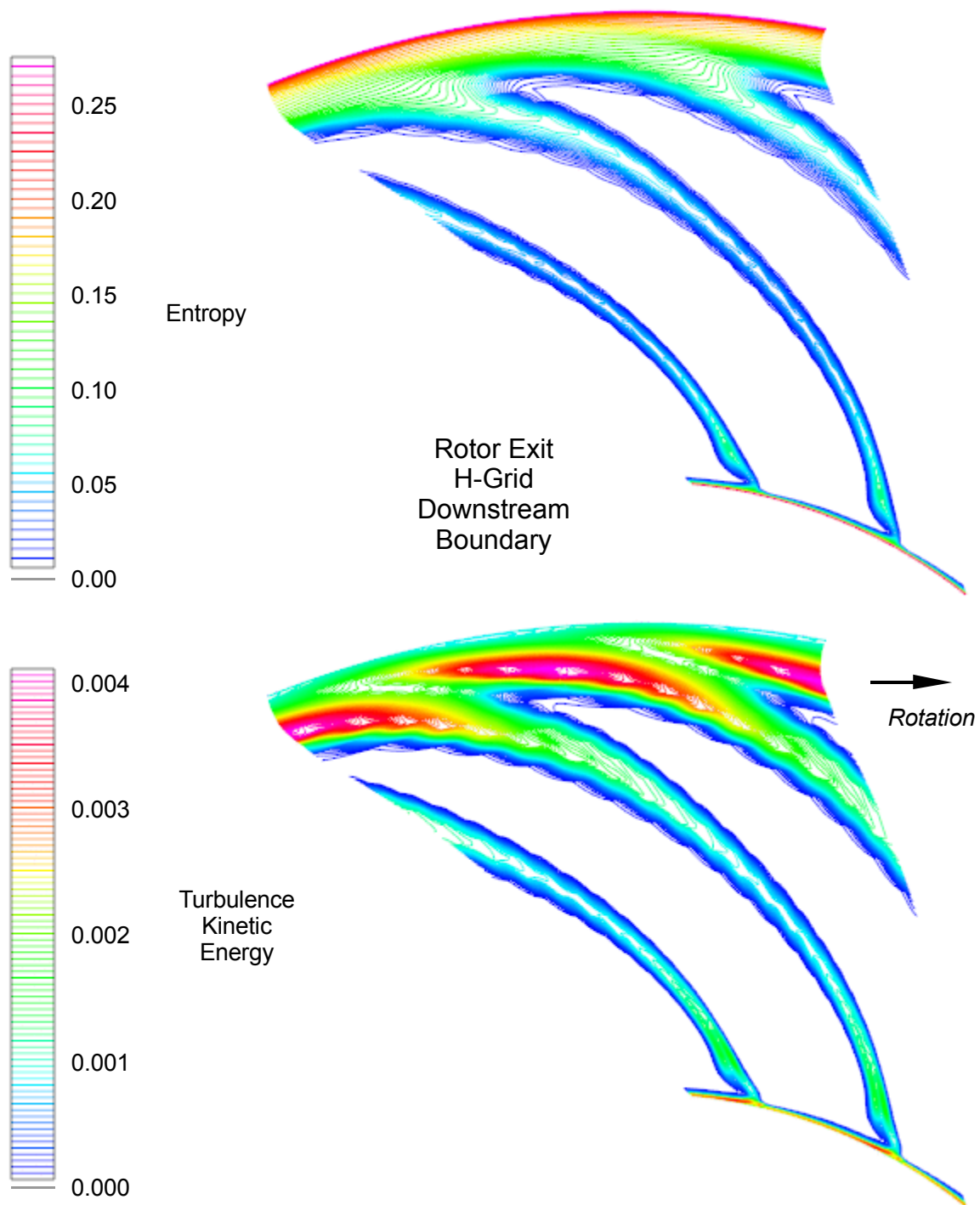
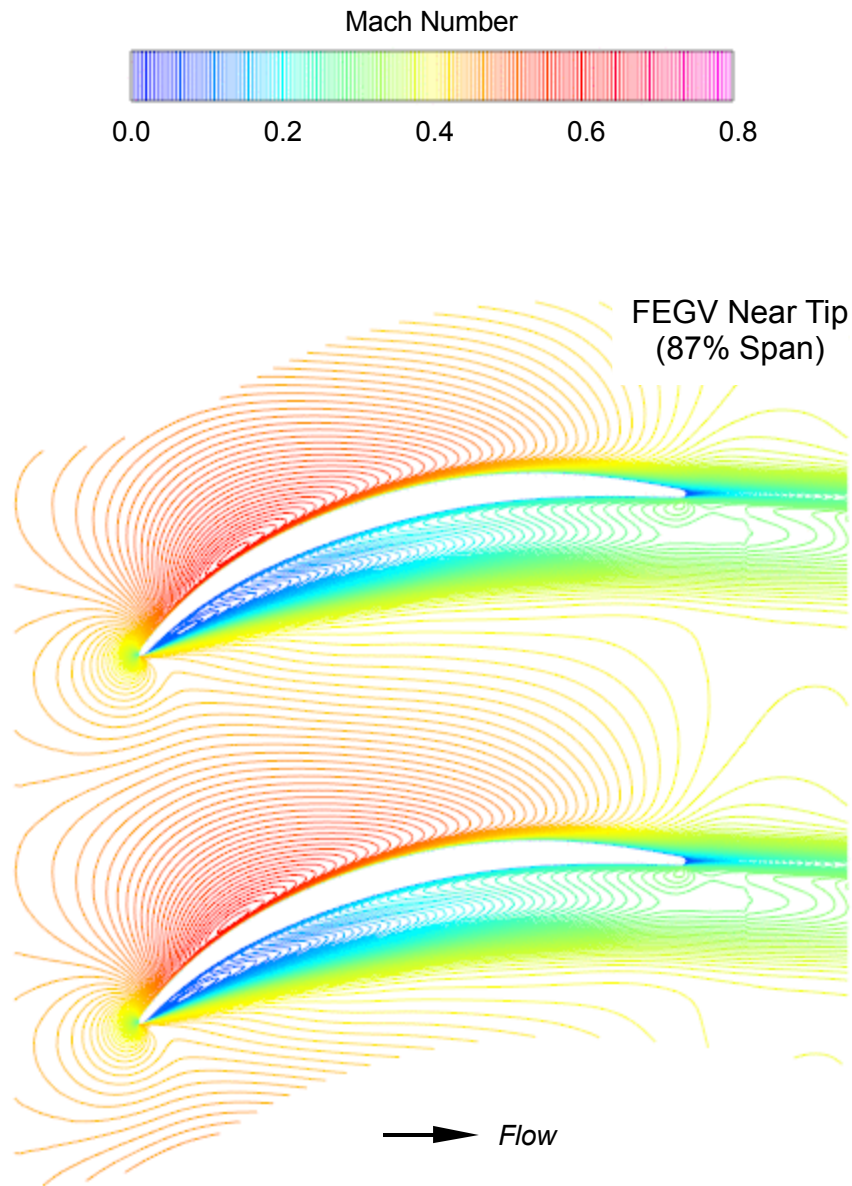


Figure 37b: Computed Rotor Flow Field for the Approach Operating Point; Downstream Mixing Plane; Entropy and Turbulence Kinetic Energy Contours

Approach Operating Point



*Figure 38a: Computed FEGV Flow Field for the Approach Operating Point;
Blade-to-Blade Mach Number Contours*

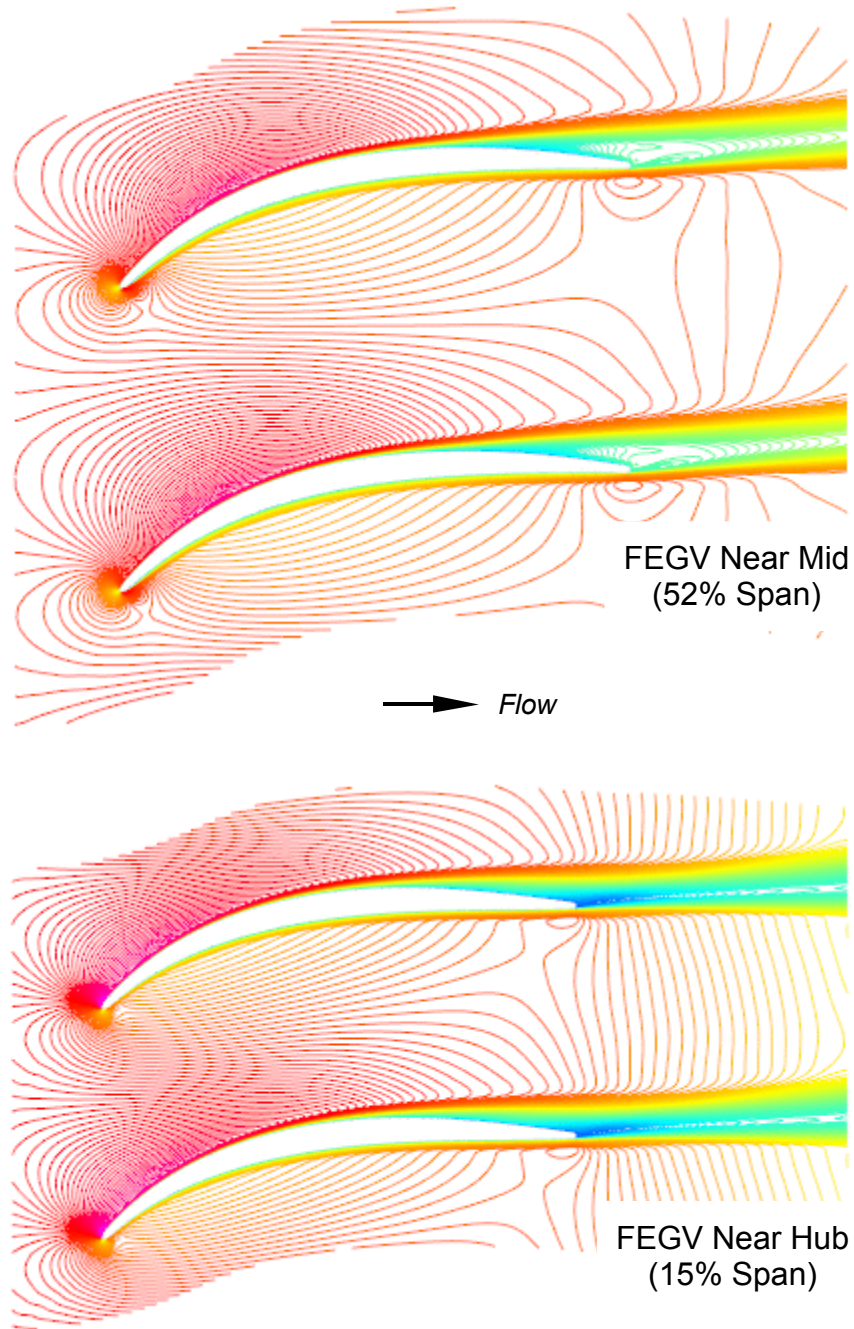


Figure 38b: Computed FEGV Flow Field for the Approach Operating Point; Blade-to-Blade Mach Number Contours

FEGV C-Grid
Downstream
Boundary

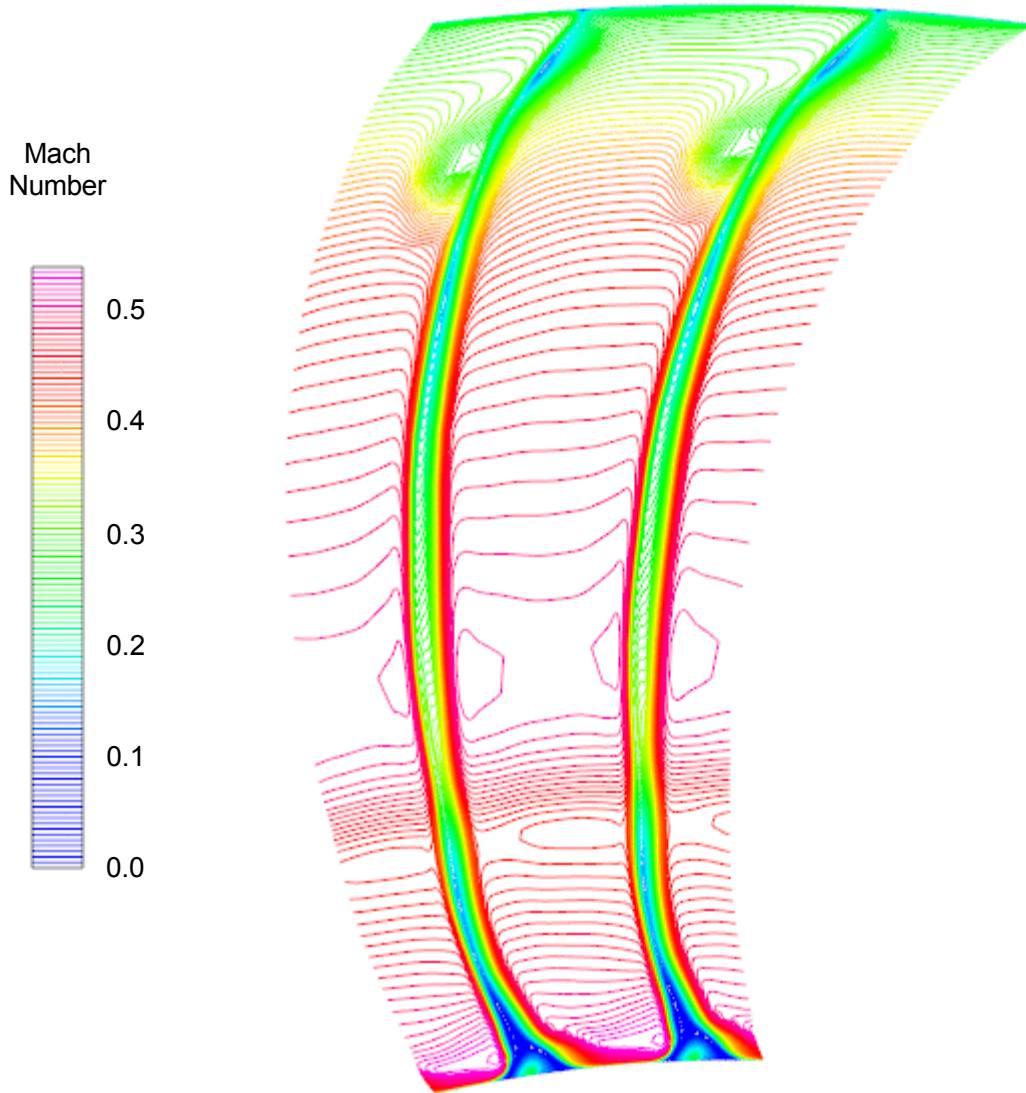


Figure 39: Computed FEGV Flow Field for the Approach Operating Point; Downstream Boundary of C-Grid; Mach Number Contours

FEGV Exit
H-Grid
Downstream
Boundary

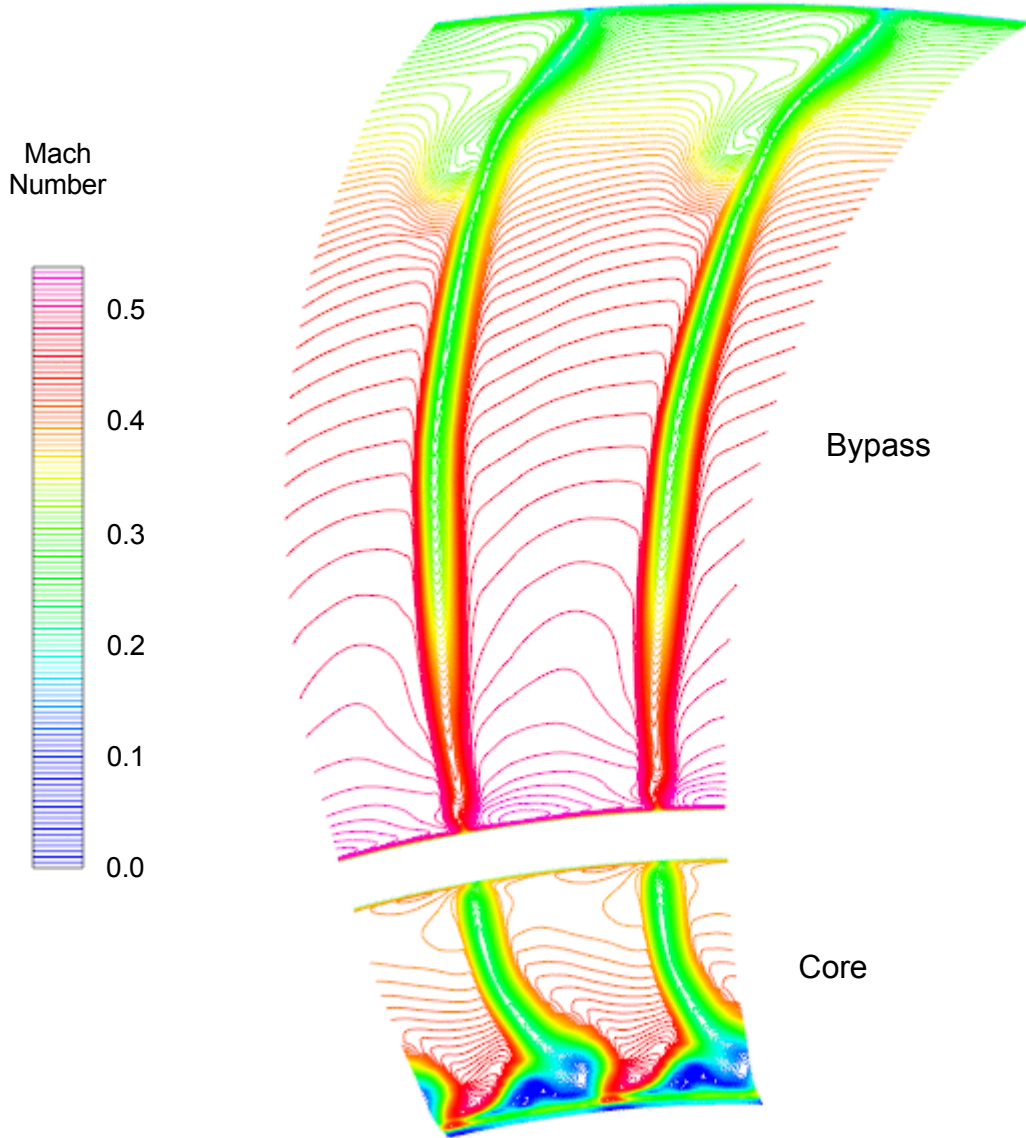


Figure 40: Computed FEGV Flow Field for the Approach Operating Point; Downstream Mixing Planes; Mach Number Contours

REPORT DOCUMENTATION PAGE			Form Approved OMB No. 0704-0188		
<p>The public reporting burden for this collection of information is estimated to average 1 hour per response, including the time for reviewing instructions, searching existing data sources, gathering and maintaining the data needed, and completing and reviewing the collection of information. Send comments regarding this burden estimate or any other aspect of this collection of information, including suggestions for reducing this burden, to Department of Defense, Washington Headquarters Services, Directorate for Information Operations and Reports (0704-0188), 1215 Jefferson Davis Highway, Suite 1204, Arlington, VA 22202-4302. Respondents should be aware that notwithstanding any other provision of law, no person shall be subject to any penalty for failing to comply with a collection of information if it does not display a currently valid OMB control number. PLEASE DO NOT RETURN YOUR FORM TO THE ABOVE ADDRESS.</p>					
1. REPORT DATE (DD-MM-YYYY) 01-10-2014	2. REPORT TYPE Final Contractor Report		3. DATES COVERED (From - To)		
4. TITLE AND SUBTITLE Computational Aerodynamic Simulations of a 1484 ft/sec Tip Speed Quiet High-Speed Fan System Model for Acoustic Methods Assessment and Development			5a. CONTRACT NUMBER NNC06BA07B		
			5b. GRANT NUMBER		
			5c. PROGRAM ELEMENT NUMBER		
6. AUTHOR(S) Tweedt, Daniel, L.			5d. PROJECT NUMBER		
			5e. TASK NUMBER NNC07E190T		
			5f. WORK UNIT NUMBER WBS 473452.02.03.07.06.01.06		
7. PERFORMING ORGANIZATION NAME(S) AND ADDRESS(ES) AP Solutions, Inc.			8. PERFORMING ORGANIZATION REPORT NUMBER E-18899		
9. SPONSORING/MONITORING AGENCY NAME(S) AND ADDRESS(ES) National Aeronautics and Space Administration Washington, DC 20546-0001			10. SPONSORING/MONITOR'S ACRONYM(S) NASA		
			11. SPONSORING/MONITORING REPORT NUMBER NASA/CR-2014-218131		
12. DISTRIBUTION/AVAILABILITY STATEMENT Unclassified-Unlimited Subject Category: 71 Available electronically at http://www.sti.nasa.gov This publication is available from the NASA Center for AeroSpace Information, 443-757-5802					
13. SUPPLEMENTARY NOTES					
14. ABSTRACT Computational Aerodynamic simulations of a 1484 ft/sec tip speed quiet high-speed fan system were performed at five different operating points on the fan operating line, in order to provide detailed internal flow field information for use with fan acoustic prediction methods presently being developed, assessed and validated. The fan system is a sub-scale, low-noise research fan/nacelle model that has undergone experimental testing in the 9- by 15-foot Low Speed Wind Tunnel at the NASA Glenn Research Center. Details of the fan geometry, the computational fluid dynamics methods, the computational grids, and various computational parameters relevant to the numerical simulations are discussed. Flow field results for three of the five operating points simulated are presented in order to provide a representative look at the computed solutions. Each of the five fan aerodynamic simulations involved the entire fan system, which includes a core duct and a bypass duct that merge upstream of the fan system nozzle. As a result, only fan rotational speed and the system bypass ratio, set by means of a translating nozzle plug, were adjusted in order to set the fan operating point, leading to operating points that lie on a fan operating line and making mass flow rate a fully dependent parameter. The resulting mass flow rates are in good agreement with measurement values. Computed blade row flow fields at all fan operating points are, in general, aerodynamically healthy. Rotor blade and fan exit guide vane flow characteristics are good, including incidence and deviation angles, chordwise static pressure distributions, blade surface boundary layers, secondary flow structures, and blade wakes. Examination of the computed flow fields reveals no excessive or critical boundary layer separations or related secondary-flow problems, with the exception of the hub boundary layer at the core duct entrance. At that location a significant flow separation is present. The region of local flow recirculation extends through a mixing plane, however, which for the particular mixing-plane model used is now known to exaggerate the recirculation. In any case, the flow separation has relatively little impact on the computed rotor and FEGV flow fields.					
15. SUBJECT TERMS Low noise; Models; Scale models; Turbofans; Acoustic measurement; Aerodynamic characteristics					
16. SECURITY CLASSIFICATION OF:			17. LIMITATION OF ABSTRACT	18. NUMBER OF PAGES	19a. NAME OF RESPONSIBLE PERSON
a. REPORT	b. ABSTRACT	c. THIS PAGE			STI Help Desk (email: help@sti.nasa.gov)
U	U	U	UU	64	19b. TELEPHONE NUMBER (include area code) 443-757-5802

